List of publications and patents of Sai Kumari Vechalapu

Publications

1. **Sai Kumari Vechalapu***, Rakesh Kumar*, Sharad Sachan, Kanchan Shaikh, Amarjyoti Mahapatra, Apparao Draksharapu, Dharmaraja Allimuthu "Organocopper and manganese complexes of pyridinecarboxaldimine induce oxidative cell death in cancer cells" (Manuscript under review in ACS Applied Bimateirals, * co-first authors)

2. Sona Tiwari, Sathyapriya Senthil, Shweta Khanna, Santhosh Duraisamy, **Sai Kumari Vechalapu**, Sharath Chandra Mallojjala, Dharmaraja Allimuthu "Tuning isatoic anhydrides' lysine ligation chemistry for bioconjugation and drug delivery" (Manuscript under revision in Cell Reports Physical Science)

3. Raju Eerlapally, **Sai Kumari Vechalapu**, Santosh Duraisamy, Divya Lakshmi Hareendran, Jayashrita Debnath, Dharmaraja Allimuthu, Apparao Draksharapu, "A Cu(II) pseudopeptide complex: a surrogate to a *formal* Cu(III) species in water and an inhibitor of cancer cell proliferation" *Inorganic Chemistry Frontiers*, (**2024**)

4. **Sai Kumari Vechalapu**, Rakesh Kumar, Niranjan Chatterjee, Sikha Gupta, Shweta Khanna, Pooja Yedehalli Thimmappa, Sathyapriya Senthil, Raju Eerlapally, Manjunath B. Joshi, Santosh K. Misra, Apparao Draksharapu, Dharmaraja Allimuthu "Redox Modulator Iron Complexes Trigger Intrinsic Apoptosis Pathway in Cancer Cells" *iScience* (**2024**, 109899)

5. Pragya Arora, **Sai Kumari Vechalapu**, Santhosh Duraisamy, Dharmaraja Allimuthu, Apparao Draksharapu "A.Pivotal Role of Salicylates in Tuning the Formation and Reactivity of Mn (V)= O's" *European Journal of Inorganic Chemistry*, (**2024**, e202400079)

6. Dharmendra Yadav, Sona Tiwari, Sathya Senthil, **Sai Kumari Vechalapu**, Santhosh Duraisamy, Viral Rawat, Dharmaraja Allimuthu, "Diazepam-based covalent modifiers of GPX4 induce ferroptosis in liver cancer cells" *Chemical Communications* (**2024**)

7. Pragya Arora, **Sai Kumari Vechalapu**, Rakesh Kumar, Ayushi Awasthi, Sathya Senthil, Dharmaraja Allimuthu, Apparao Draksharapu "Mn (II) Polypyridyl Complexes: Precursors to High Valent Mn(V)=O Species and Inhibitors of Cancer Cell Proliferation" *Chemistry–A European Journal* (**2023**, *29*(53), e202301506)

8. Revathy Sahadevan, Anupama Binoy, **Sai Kumari Vechalapu**, Pandurangan Nanjan, Sushabhan Sadhukhan "*In situ* global proteomics profiling of EGCG targets using a cell-permeable and Click-able bioorthogonal probe" *International Journal of Biological Macromolecules* (**2023**, *237*, 123991)

Patents

1. 2-Amino benzophenone derivatives for targeted ferroptosis induction in cancer therapy. Dharmaraja Allimuthu, Sai Kumari Vechalapu, Shweta Khanna, Sona Tiwari, Dharmendra K Yadav, India, 202311063839, **17/112023**

Manuscripts under preparation

1. **Sai Kumari Vechalapu**, Santhosh Duraisamy, Rakesh Kumar, Sathya Senthil, Deepa Anjar, Dharmaraja Allimuthu, Apparao Draksharapu, Suresh Kumar "Small molecule-mediated accumulation of lipid globules drives lysophagy through mitochondrial dysfunction to prevent liver cancer cell proliferation"

2. **Sai Kumari Vechalapu**, Sikha Gupta, Dharmaraja Allimuthu, Apparao Draksharapu "Copper accumulation by an ionophore induces protein phase condensation and inhibits the progression of osteosarcoma cells"

Article

Redox modulator iron complexes trigger intrinsic apoptosis pathway in cancer cells
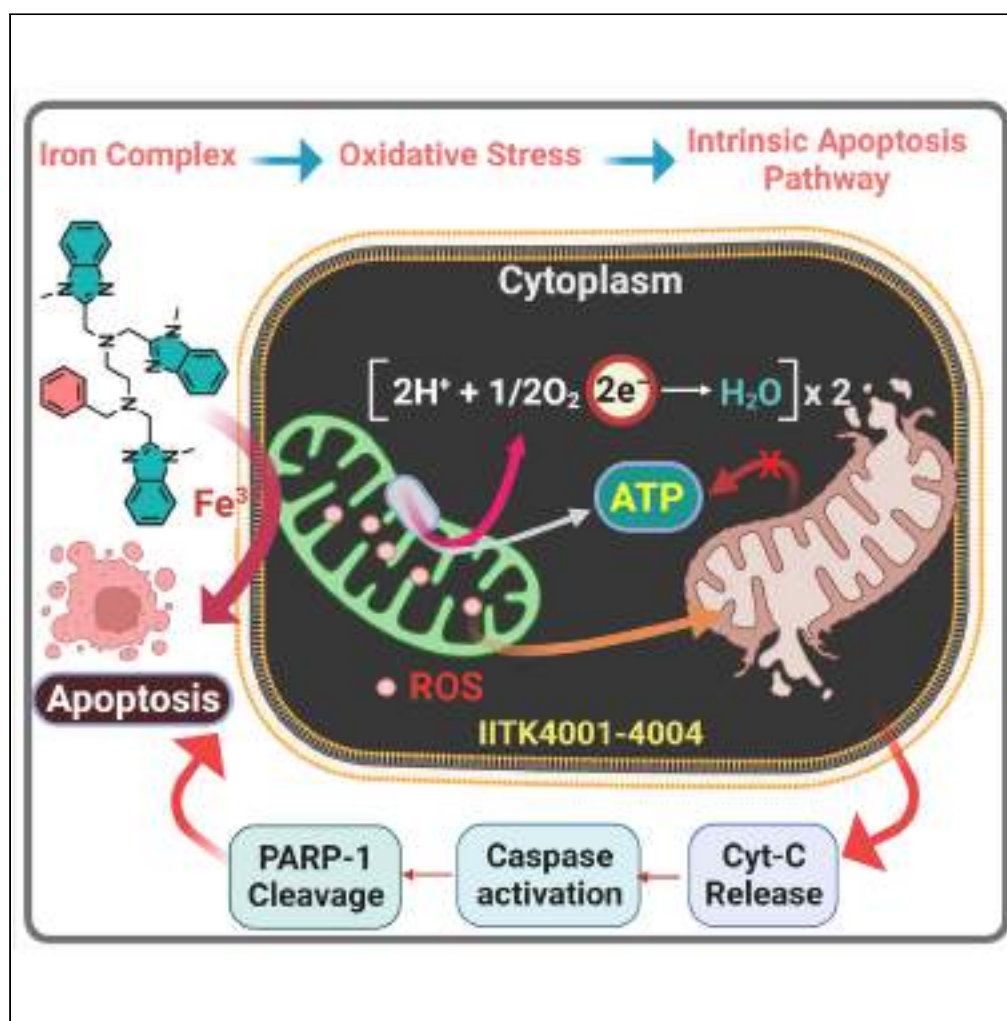
Sai Kumari Vechalapu, Rakesh Kumar, Niranjan Chatterjee, ..., Santosh K. Misra, Apparao Draksharapu, Dharmaraja Allimuthu

skmisra@iitk.ac.in, appud@iitk.ac.in, atdharma@iitk.ac.in

Highlights

Cancer's drug resistance spurs need for new therapies

Iron chelators halt liver cancer growth via redox disruption

Iron complexes induce oxidative stress, triggering apoptosis

Exploiting iron overload, a unique anticancer strategy

Article

Redox modulator iron complexes trigger intrinsic apoptosis pathway in cancer cells

Sai Kumari Vechalapu,[1] Rakesh Kumar,[1] Niranjan Chatterjee,[2] Sikha Gupta,[1] Shweta Khanna,[1] Pooja Yedehalli Thimmappa,[3] Sathyapriya Senthil,[1] Raju Eerlapally,[1] Manjunath B. Joshi,[3] Santosh K. Misra,[2,*] Apparao Draksharapu,[1,*] and Dharmaraja Allimuthu[1,4,*]

SUMMARY

The emergence of multidrug resistance in cancer cells necessitates the development of new therapeutic modalities. One way cancer cells orchestrate energy metabolism and redox homeostasis is through overloaded iron pools directed by iron regulatory proteins, including transferrin. Here, we demonstrate that targeting redox homeostasis using nitrogen-based heterocyclic iron chelators and their iron complexes efficiently prevents the proliferation of liver cancer cells (EC$_{50}$: 340 nM for IITK4003) and liver cancer 3D spheroids. These iron complexes generate highly reactive Fe(IV)=O species and accumulate lipid peroxides to promote oxidative stress in cells that impair mitochondrial function. Subsequent leakage of mitochondrial cytochrome c activates the caspase cascade to trigger the intrinsic apoptosis pathway in cancer cells. This strategy could be applied to leverage the inherent iron overload in cancer cells to selectively promote intrinsic cellular apoptosis for the development of unique iron-complex-based anticancer therapeutics.

INTRODUCTION

Cancer is the leading source of deaths worldwide, and the emergence of drug resistance to the existing class of anticancer therapeutics warrants novel therapeutic interventions. While organic small molecule therapeutics continue to dominate the medicinal chemistry, milestone therapeutic cisplatin is crowned as the major metal-based therapeutic to rule cancer therapy for the past four decades.[1] Apart from cisplatin,[1] carboplatin and oxaliplatin are the follow-up platinum drugs widely used for treating cancer. These molecules predominantly function through the plastination of DNA (deoxyribonucleic acid) by intrastrand cross-linking of deoxyguanosine residues in cells among several other mechanisms.[2] Metal-based therapeutics that operate beyond DNA targeting mechanisms in cancer cells could serve as potential alternatives to strengthen the arsenal of metal-based anticancer drugs.[3–12] Beyond cisplatin- or platinum-based anticancer drugs, several gold- and ruthenium-based cancer therapeutics are in the clinical trials. Several iron complexes including iron-ferrocene and imine complexes exhibit submicromolar potency and function through the induction of reactive oxygen species (ROS) in cancer cells for their mechanism of action.[13–16] These compounds represent a novel avenue for therapeutic development in oncology, offering diverse mechanisms for targeting malignant cells.

Metal ion homeostasis is essential for cell signaling, growth, survival, and metabolism.[17] Particularly, systemic functions and metabolism of iron are regulated by ferroportin and iron-regulatory proteins.[17] Transferrin, iron-responsive element-binding proteins (IRPs), and iron-sulfur cluster proteins (ISCs) transfer and regulate iron homeostasis in cells, which are critical for oxygen transport, respiration, cell signaling, proliferation, and metabolism.[18] However, the accumulation of free iron and disruption of its homeostasis is recorded in several cancers and other diseases.[17,19,20] The ROS-generating capability of free iron pools, leading to DNA damage and mutations, is well characterized as a responsible factor for cancer onset and progression.[21] In parallel, a high level of iron is essential for balancing the fast metabolism and respiration in cancer cells, for example, bone and liver cancer cells are known to possess high iron content than their respective normal cells.[21–24] Trapping intracellular metal ions using organic ligands has proved successful in eliminating the tumor.[25–27] Instead of oxidative phosphorylation in mitochondria, cancer cells depend on aerobic glycolysis for energy production called "Warburg effect," an ineffective process to produce ATP.[28] Therefore, a disruption of this oxidative metabolism by depleting intracellular iron would make the cancer cells vulnerable to iron chelators. We hypothesized to additionally challenge the cancer cell survival by turning its intracellular iron into an iron complex capable of generating deleterious ROS that could promote oxidative cell death. Here, we report the identification of iron complexes and their ligands, nitrogen-based heterocyclic scaffolds chelating with iron, that oxidatively impair mitochondrial function to trigger intrinsic apoptosis pathway in cancer cells.

[1]Department of Chemistry, Indian Institute of Technology Kanpur, Uttar Pradesh 208016, India
[2]Department of Biological Sciences and Bioengineering, Indian Institute of Technology Kanpur, Uttar Pradesh 208016, India
[3]Department of Ageing Research, Manipal School of Life Sciences, Manipal Academy of Higher Education, Manipal 576104, India
[4]Lead contact
*Correspondence: skmisra@iitk.ac.in, appud@iitk.ac.in, atdharma@iitk.ac.in
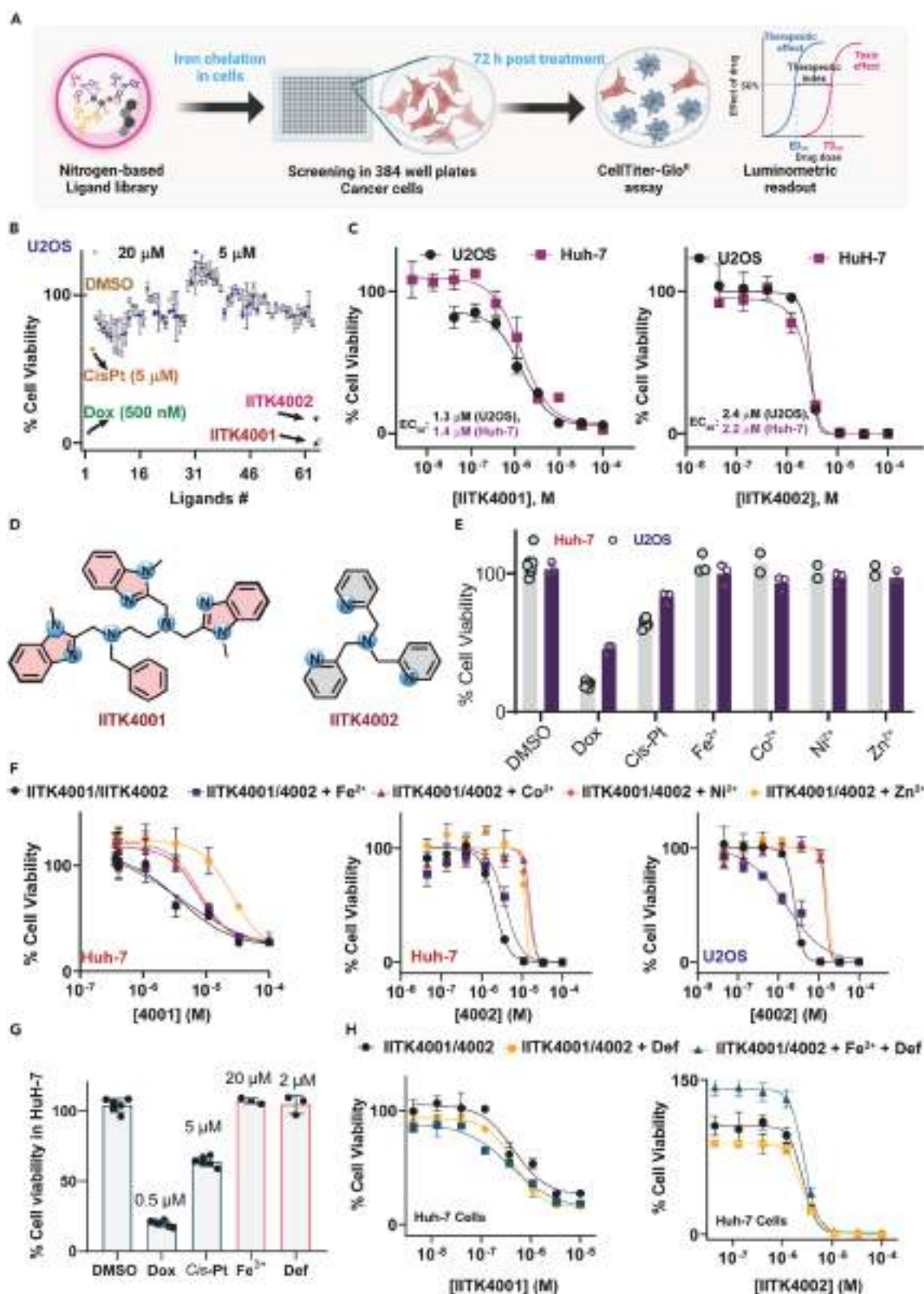https://doi.org/10.1016/j.isci.2024.109899

Figure 1. IITK4001 and IITK4002 promote antiproliferative activity against Huh-7 and U2OS cells with iron salt

(A) Schematic flow of ligand screening in a cell viability assay using a luminescence-based Celltiter-Glo assay after 72 h of treatment.

(B, C, E, F) Cell viability data: screening of ligand library (#75) at 20 and 5 μM (only screened in U2OS cells) (B), dose-dependent analysis of IITK4001 and IITK4002(U2OS and Huh-7) (C), treatment of metal salts alone (20 μM, Huh-7 and U2OS cells) (E), and metal salts in combination with IITK4001 (Huh-7 cells) or IITK4002 (Huh-7 and U2OS cells) (F).

(D) Structures of lead ligand scaffolds IITK4001 and IITK4002.

(G and H) Antiproliferative activity of IITK4001/4002 in combination with deforoxamine (Def) and iron salt in Huh-7 cells. All graphs indicate mean ± SD. Data presented are performed in two independent cell lines and are representative of more than two independent experiments with a minimum of three technical replicates. Cell viability data are normalized relative to DMSO treatment control as 100%.

RESULTS

IITK4001 and IITK4002 traps iron and complexes to prevent cancer cell proliferation

We first synthesized ligand scaffolds (di-, tri-, tetra-, and pentadentate) on one condition that they are not planar but possess versatile three-dimensional orientations to resist DNA intercalation. Our screening of a ligand library (75 scaffolds, 20 and 5 μM) identified two hit molecules—N'-benzyl-N',N''-(tris-N-methylbenzimidazole)-ethylenediamine, IITK4001 and tris(2-pyridylmethyl)amine, IITK4002—as a potent inhibitors of osteosarcoma (U2OS) cell proliferation (Figures 1A and 1B). Both IITK4001 and IITK4002 dose-dependently inhibited the proliferation of hepatocellular carcinoma (Huh-7) and U2OS cell growth with a range of 1–2 μM EC_{50} (Figures 1C and 1D). These are nitrogen-based heterocyclic molecules, capable of acting as chelators for various metal ions[29]; therefore, we determined to investigate the role of metal complexation with 3d metals (iron, cobalt, nickel, and zinc) in the antiproliferative activity of IITK4001 and IITK4002. Hence, we treated the cells with our lead molecules alone or in combination with indicated metal salts at non-toxic concentrations (20 μM; Figure 1E). Interestingly, iron salts cotreatment with both IITK4001/IITK4002 retained or had minimal effect on the antiproliferative potential. However, other metal salts were found to suppress the activity of ligands IITK4001/IITK4002 when combined (Figure 1F). Next, to investigate whether iron depletion using our metal ion chelators in cells alone is sufficient to prevent cancer cell proliferation, we performed combination experiments with deforoxamine (Def, an iron chelator; Figures 1G and S13) at the non-toxic concentration (2 μM). We observed no substantial change in the cell survival in combination when compared to the lone treatment conditions. Yet, the addition of excess iron salt to IITK4001/4002 or in combination with Def did not rescue the cell death (Figure 1H). Therefore, we concluded the causative agent of cell death is unlikely to be iron depletion alone, rather a shift in the free iron pool to form a complex of IITK4001/4002 and a possibility of additional roles for these iron complexes in the antiproliferative activity anticipated.

Reversible cross-complexation studies of IITK4002 with Fe^{2+} and other biologically relevant metal ions

The initial examination of IITK4001 and IITK4002 led to the conclusion of iron complex formation rather than iron depletion as the dominant mechanism for preventing cancer cell proliferation. However, other metal ions in the biological system could potentially interfere with the activity. Therefore, we assembled salts of various metal ions around their physiological concentrations including alkali metals, 5 mM solution of sodium, magnesium, potassium, calcium salts, and d-block transition metals such as manganese (1 μM), iron (20 μM), cobalt (0.5 μM), nickel (0.5 μM), copper (5 μM), and zinc (100 μM) salts (Figure 2).[26] Due to the solubility issues with IITK4001 under physiological conditions, we restricted all our cross-complex formation studies with IITK4002 (Figure 2). Initially, we monitored the Fe(II)-IITK4002 formation with 0.2–2.0 equiv. of IITK4002 using UV-visible spectroscopy by following a distinct absorption at 395 nm (Figures 2A–2C). We find an instant complex formation upon the addition of Fe^{2+} to IITK4002, and this was found to be saturated with 1:1 stoichiometry, indicating the 1 to 1 complex formation. This complex was found to be irreversible and stable in the complexation medium for more than an hour (Figures 2A and 2B). To study the interference of assembled biologically relevant metal ions, an excess of these metal salts (5 equiv.) was added to the preformed Fe(II)-IITK4002 complex and monitored the change in absorbance at 395 nm. We noted no effect with any of the alkali metal ions and also with transition metal ions such as Mn^{2+}, Ni^{2+}, and Co^{2+} salts, indicating Fe(II)-IITK4002 complex is irreversible under these conditions (Figures 2D and 2E). However, we find a slow equilibration of Fe(II)-IITK4002 with Zn^{2+} over 60 min to a ~50% Fe(II)-IITK4002 (Figure 2F). Conversely, the reverse addition of Fe^{2+} salt to preformed Zn(II)-IITK4002 exhibited a rapid displacement of Zn^{2+} within a few seconds ($t_{1/2}$ = 4 s) to form Fe(II)-IITK4002 and observed a slow equilibration over 60 min (Figure 2G), thereby suggesting the complex is competitively reversible. Identical to this, the addition of Cu^{2+} was found to react instantly with Fe(II)-IITK4002 that in less than 20 s all the Fe(II)-IITK4002 converted into Cu(II)-IITK4002 ($t_{1/2}$ = 8.3 s; Figures 2H and 2I) and was found to equilibrate to nearly 50% in 6 min. Likewise, the reverse addition also exhibited a similar trend of instant conversion of Cu(II)-IITK4002 to Fe(II)-IITK4002 transformation ($t_{1/2}$ = 3.2 s; Figure 2J). Together, the cross-complexation studies with biologically relevant metal ions indicate that Fe(II)-IITK4002 remain unaffected with other metal ions tested, and Zn^{2+} and Cu^{2+} could potentially interfere. While the physiological concentration of copper (0.5 μM) is 4-fold lesser than iron concentration (20 μM), zinc (100 μM) level is found to be 5-fold higher than iron. Despite higher levels of Zn^{2+} in the biological systems, we have observed addition of Zn^{2+} to IITK4001 showed more of a preventive role than retaining or enhancing the cell death induced by IITK4002 (Figure 1F). The abovementioned set of experiments have clearly ruled out the majority of the biologically relevant metal ions except for a competition between Fe^{2+} and Cu^{2+}. Therefore, evaluating the individual effects of Fe^{2+} and Cu^{2+} ions on IITK4002 is essential to precisely capture the metal ion responsible for the antiproliferative activity of our lead ligand molecules.

Synthesis and physio-chemical evaluation of iron complexes (IITK4003 and IITK4004) and other 3d-metal complexes

Iron and copper are indispensable elements for redox homeostasis in cells due to their versatile redox capacity to switch between multiple oxidation states.[5,25–27,30–33] Next, we set out to investigate whether the effect of our ligands is due to their complexation with Fe^{2+} or Cu^{2+}. To
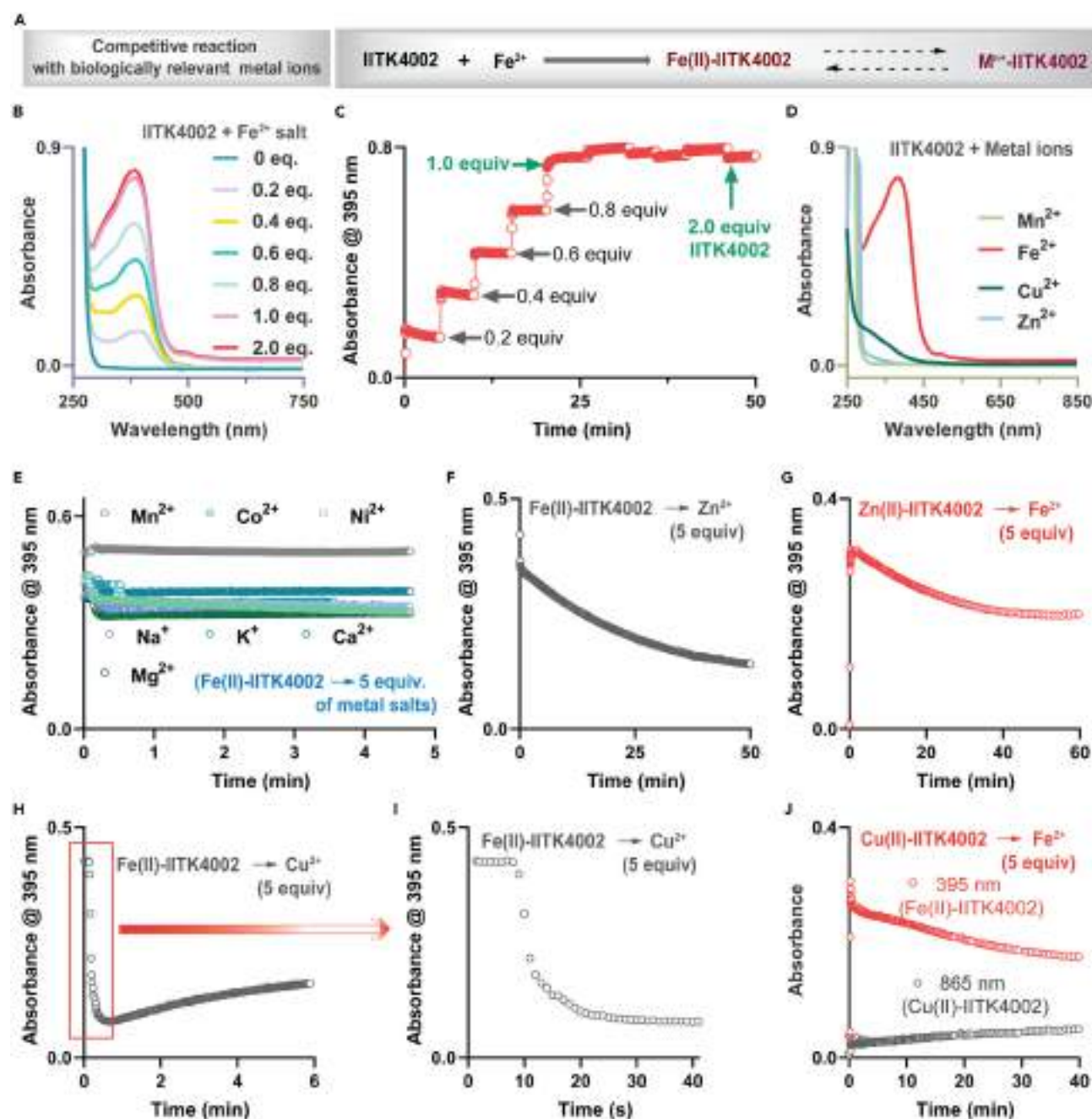
Figure 2. Fe(II)-IITK4002 is competitively reversible with Zn^{2+} and Cu^{2+} salts

(A) Scheme for competitive complexation studies for IITK4002 with Fe^{2+} and other metal ions.

(B–D) UV-visible spectra of IITK4002 with Fe^{2+} salt ([FeII(H_2O)$_6$](ClO_4)$_2$ (0 to 2.0 equiv.; B and C) and other metal salts (1 equiv., D) in 1:1 acetonitrile: water at RT.

(E, F, H, I) Absorbance was recorded at 395 nm for Fe(II)-IITK4002 after exposing it to indicated metal salts (5 equiv.) at RT. Metal salts: ZnII(OTf)2, CuII(H_2O)$_6$(ClO_4)$_2$, CoII(H_2O)$_6$(ClO_4)$_2$, NiII(H_2O)$_6$(ClO_4)$_2$, MnII(H_2O)$_6$(ClO_4)$_2$, NaCl, KCl, $CaCl_2$, and $MgSO_4$.

(G and J) Zn(II)-IITK4002 (g) or Cu(II)-IITK4002 (j) complex exposed to Fe^{2+} salt (5 equiv.) at RT and absorbance recorded at 395 nm for the Fe(II)-complex formation.

unambiguously characterize this, we synthesized the iron complexes IITK4003 and IITK4004 and characterized them by various spectroscopic techniques and X-ray crystallography studies (Figures 3 and S1–S5; Scheme S1, S2, Table S1).[33–35] Iron complexes IITK4003 and IITK4004 were found to show comparable growth inhibition activity against both Huh-7 and U2OS cells as in the ligands treatment alone (Figures 3A and 3B). Remarkably, IITK4003 exhibited an exceptional antiproliferative activity with an EC_{50} of 340 nM against Huh-7 cells, a 3-fold better than the
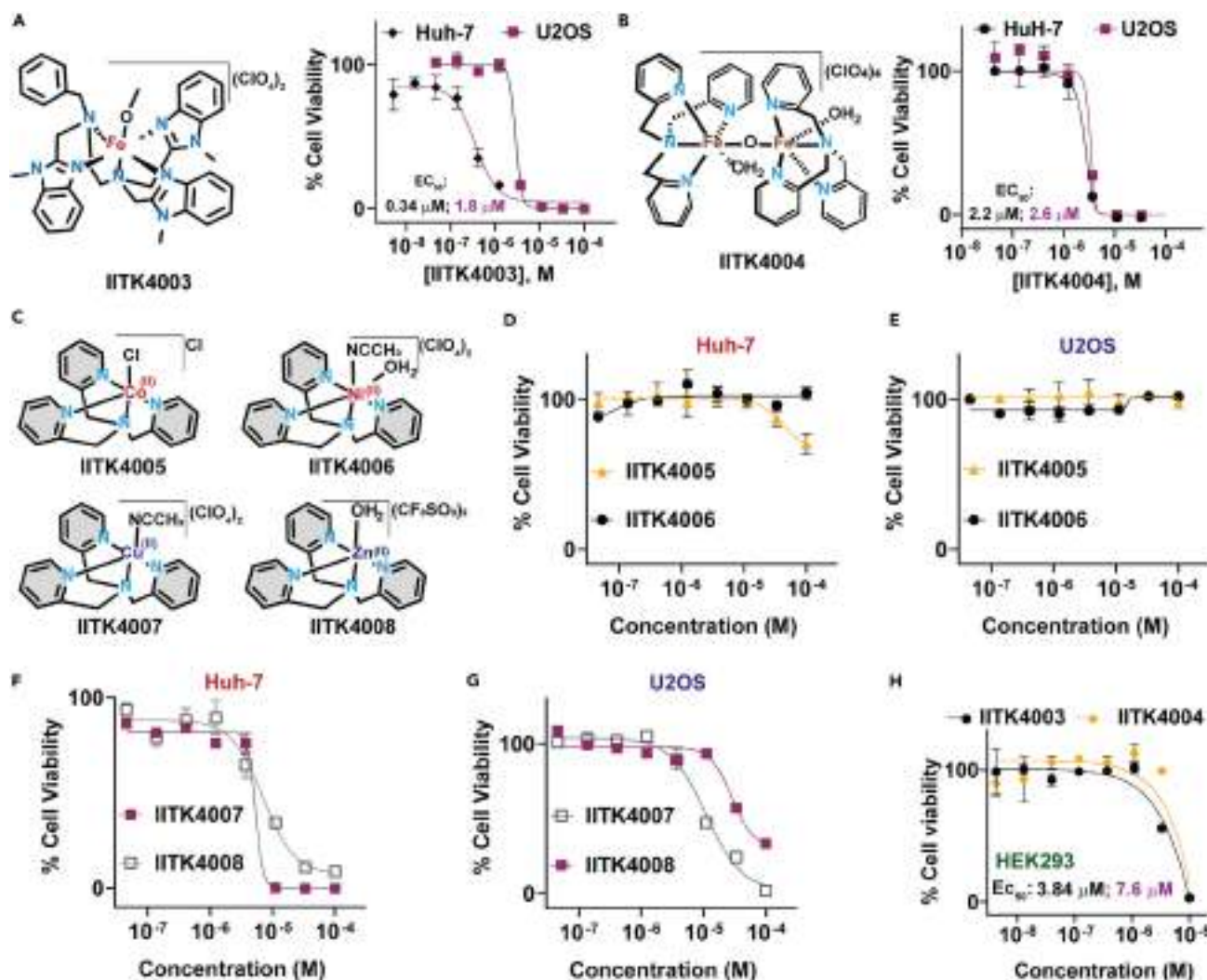
Figure 3. Iron complexes (IITK4003/4004) exhibit potent antiproliferative activity over other metal complexes in Huh-7 cells

(A–G) Cell viability of Huh-7 and U2OS cells assessed when treated with IITK4003 (A), IITK4004 (B), and IITK4005-4008 (D–G) using Celltiter-Glo assay and the structure of metal complexes studied here are given (A–C).

(H) The toxicity of lead complexes, IITK4003/4004, to HEK293 cells was assessed in a dose-dependent fashion. Graphs A, B, D–H indicate mean $\pm$ SD. Data presented are performed in two independent cell lines and are representative of more than two independent experiments with a minimum of three technical replicates. Cell viability data are normalized relative to DMSO treatment control as 100%.

parent ligand IITK4001 (Figure 3A). This difference in potency could be partially attributed to the better solubility of the complex over the ligand in aqueous conditions. Next, we synthesized authentic metal complexes of IITK4002 with other 3d-metal salts, Co^{2+} (IITK4005), Ni^{2+} (IITK4006), Cu^{2+} (IITK4007), and Zn^{2+} (IITK4008) (Figure 3C). The complexation of these 3d-metal ions with IITK4001 failed due to experimental difficulty in crystallizing and obtaining pure complexes. Then, we evaluated for their ability to prevent the growth of Huh-7 and U2OS in a dose-dependent fashion. In our evaluation for the antiproliferative activity of IITK4005 and IITK4006, both were found to be non-toxic even at 100 μM concentrations (Figures 3C–3E), suggesting Co^{2+} and Ni^{2+} complexation is unlikely to be responsible for the ligand's antiproliferative activity. Interestingly, two of the metal ions found to be competitive in complexing with IITK4002, Cu^{2+} (IITK4007) and Zn^{2+} (IITK4008), exhibited a weak potency (5.4 μM, 7 μM in Huh-7, and 12.8 μM and >50 μM in U2OS for IITK4007 and IITK4008, respectively) in preventing the growth of cancer cells evaluated. However, the antiproliferative potencies were significantly lower than the parent ligand alone or the respective iron complex, IITK4004 (Figures 3C, 3F, and 3G). Together, the evaluation of metal complexes and the combination of various metal salts with heterocyclic ligands highlight that their antiproliferative activity arises predominantly due to iron complex formation in cells. Next, we extended the cell viability assay in the human embryonic kidney (HEK293) to estimate the selectivity index (SI) of our lead complexes (IITK4003 and IITK4004). We recorded an EC_{50} of 3.82 μM for IITK4003 with HEK293 cells, an estimated SI of 9.0 (EC_{50} in 0.34 μM), and an SI of 3.4 for Huh-7 cells (EC_{50}: 7.6 μM with HEK293 cells and 2.2 μM with Huh-7 cells, Figure 3H). Overall, IITK4003/4004 showed better
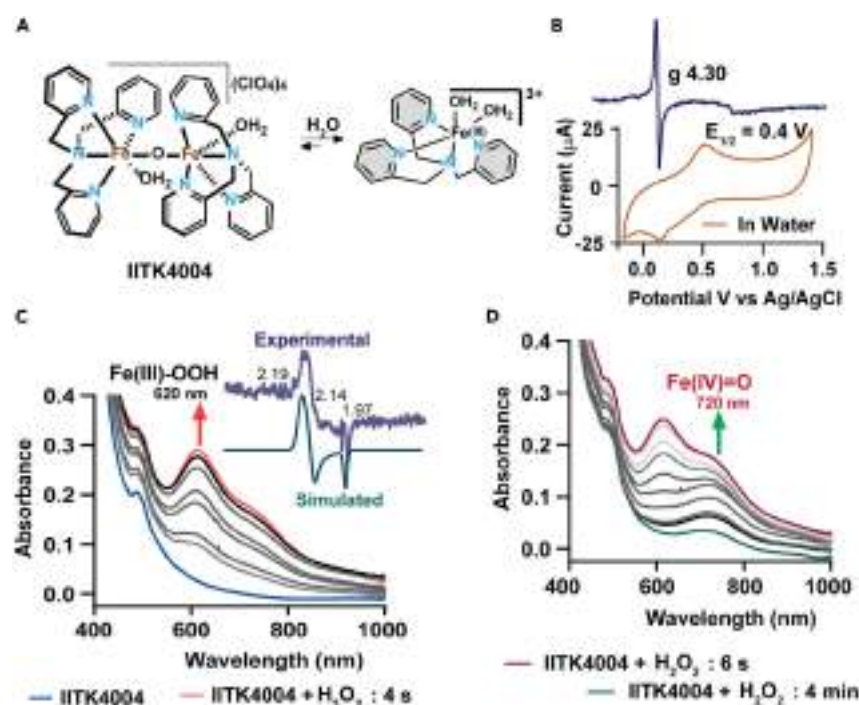
Figure 4. Iron complex, IITK4004, generates reactive metal-oxo species under simulated physiological conditions

(A and B) Monomerization of IITK4004 in water assessed using X-band EPR spectrum of IITK4004 in water/CH3CN at 120 K (insert) and cyclic voltammogram in water.

(C) UV/Vis absorption spectral studies depicting reactive meta-oxo species formation ([(TPA)Fe(III)-OOH]2+ (620 nm) and its X-band EPR spectrum compared with simulated EPR spectrum (insert).

(D) The transformation of [(TPA)(III)Fe-OOH]$^{2+}$ (620 nm) to [(TPA)Fe(IV) = O]$^{2+}$ (720 nm) in a reaction of IITK4004 with H2O2 (10 equiv.) in water is monitored using UV/Vis absorption spectral studies.

selectivity in preventing liver cancer cells' growth (Huh-7) over normal kidney cells. These studies together suggested that the complexation of iron with IITK4001/4002 is a major determinant for the antiproliferative action in Huh-7 and U2OS cells.

IITK4003/4004 generates reactive metal-oxo species under aqueous conditions

In addition to iron depletion, we anticipated a lead redox role for our top hits' mechanism of action in cells. The redox mechanisms of Fe(II) complexes would generate ROS in cells to trigger redox imbalance. The delicate balance of redox homeostasis is essential for cancer cell survival and metastasis, which could be capitalized on for developing selective cancer therapeutics.[36–38] Therefore, we evaluated the redox reactivity of IITK4004 with peroxides in water (Figures 4A–4D and S7–S11), a study thus far not investigated, majorly owing to the instability of reactive metal-oxo species in an aqueous milieu. While we expect the dinuclear iron complex IITK4004 to be electron paramagnetic reso-nance (EPR)-silent (due to antiferromagnetic coupling), we observed a high spin S = 5/2 signal, indicative of monomeric [Fe(III)-IITK4002]$^{3+}$ formation upon dissolution (Figures 4A, 4B, and S11).[39] Our cyclic voltammetry (CV) studies of IITK4004 and *in situ* prepared Fe(II)-IITK4002 in water exhibited a reversible redox wave at E$_{1/2}$ 0.4 V vs. Ag/AgCl, whereas E$_{1/2}$ of 1.2 V vs. Ag/AgCl in acetonitrile indicated more facile oxidation in water (Figures 4A, 4B, and S7). Next, we exposed IITK4004 in water to H2O2 and observed a characteristic absorption for [(IITK4002)Fe(III)-OOH]$^{2+}$ species at 620 nm, and this species was also characterized using EPR spectroscopy (g values: 2.19, 2.14, and 1.97; Figure 4C).[39–42] Together, these data indicate that IITK4004 produces a monomeric [(IITK4002)Fe(III)-OOH]$^{2+}$ species in water upon the inter-action with H2O2. Unlike in acetonitrile (Figures S7–S11), the [(IITK4002)Fe(III)-OOH]$^{2+}$ in water converts temporally to [(IITK4002)Fe(IV) = O]$^{2+}$ with an absorption band at 720 nm (Figures 4C and 4D).[43] A similar set of reactivity patterns was observed for IITK4004 with *tert*-butyl hydro-peroxide (tBuOOH) to generate reactive oxidative species [(IITK4002)Fe(IV) = O]$^{2+}$(Figures S8D and S10).[44,45] Further, we independently mixed IITK4002 with Fe^{2+} and Fe^{3+} salts for *in situ* formation of (IITK4002)Fe(II) and (IITK4002)Fe(III) complexes. To our delight, exposing them to H2O2 and tBuOOH produced a similar Fe(III)-OOH and Fe(III)-OOtBu, respectively, which decayed to yield the highly reactive [(IITK4002)Fe(IV) = O]$^{2+}$ complex (Figures 4C, 4D, and S11). A comparable study for IITK4003 capturing metal-oxo species formation (Figure S6) has strongly suggested that both complexes possess a strong oxidative capacity with peroxides under physiological conditions.

ROS generation by IITK4001-IITK4004 accumulates lipid peroxide but no sign of DNA damage

After establishing the formation of reactive iron-oxo intermediates with peroxides under *in vitro* conditions, we assessed the cellular ROS gen-eration with our hits. Initially, we performed the Amplex Red assay to quantify extracellular ROS upon treatment of Huh-7 cells with our lead
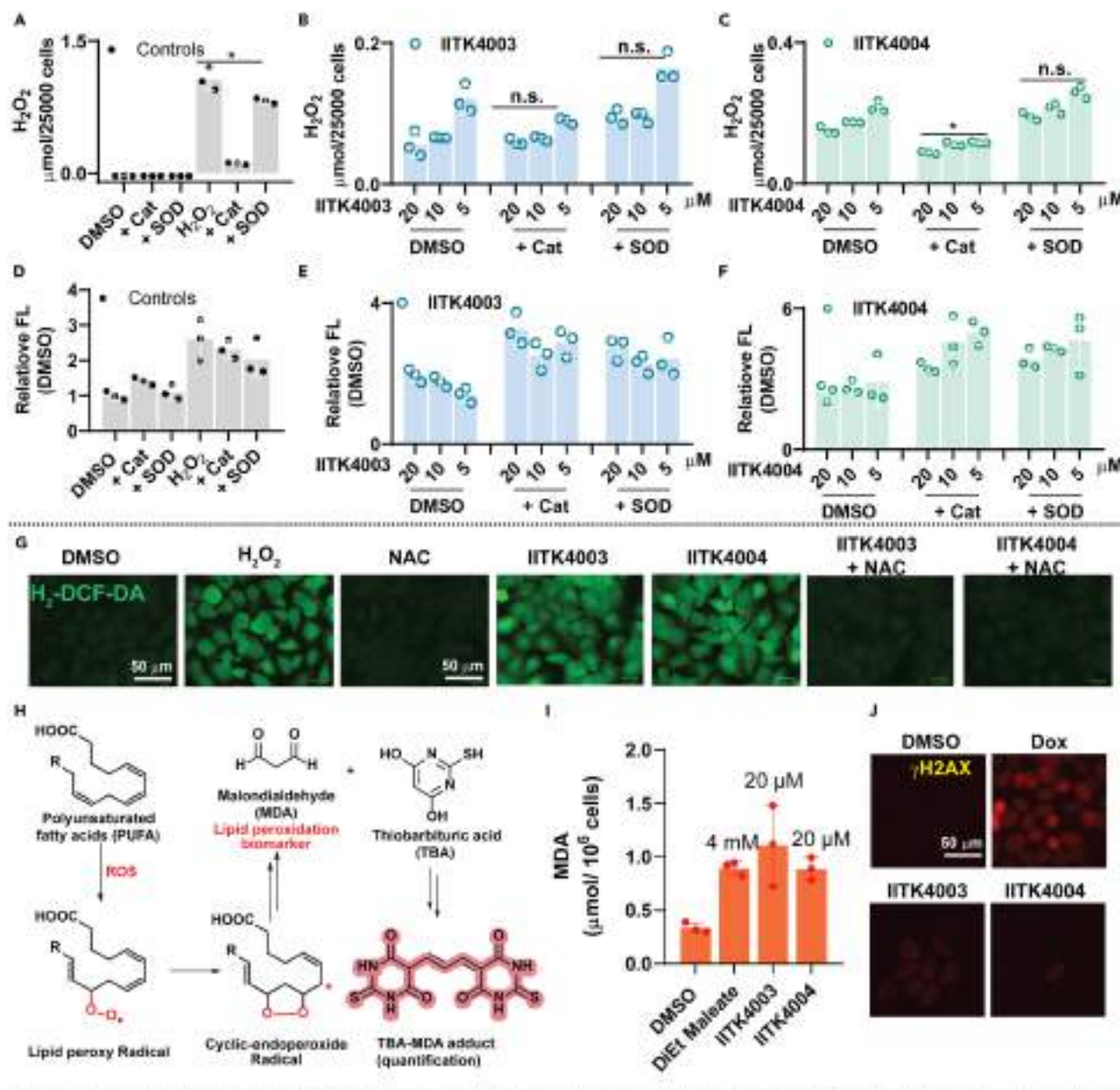
Figure 5. Lead molecules accumulate lipid peroxide to induce oxidative stress in cancer cells

(A–F) Extracellular ROS was quantified after the treatment of Huh-7 cells with IITK4003/4004 in combination with catalase and superoxide dismutase enzymes using fluorescence-based Amplex red assay (A–C) and DHE oxidation assay (D–F).

(G) Intracellular ROS accumulation was visualized using H_2-DCFDA oxidation experiment. Scale bar: 25 μm.

(H, I) Schematic depicting polyunsaturated fatty acid (PUFA, lipid) peroxidation in cells (H) and its quantification through MDA using TBARS assay (I).

(J) Immunofluorescence analysis of cells stained with anti-γH2AX upon treatment with doxorubicin (Dox) and lead molecules (20 μM). Scale bar: 25 μm. Graphs A–F and I indicate mean ± SD. Data presented are representative of more than two independent replicates and a minimum of three technical replicates.

molecules (Figures 5A–5C).[46] Indeed, our lead molecules generated ROS extracellularly and addition of catalase enzyme (a quencher of hydrogen peroxide) or superoxide dismutase enzyme (SOD, converts superoxide radical anion into hydrogen peroxide) had partial or minimal effect on the IITk4003/4004-induced ROS generation (Figures 5A–5C). We also used another fluorescence-based assay, dihydroethidine (DHE) oxidation assay for ROS measurement. The DHE reacts with superoxide radical anion to generate 2-hydroxy ethidium and hydroxy radical to generate ethidium as oxidized products.[46–48] We observed a similar trend in ROS generation as in the Amplex Red assay that our lead molecules profoundly generated ROS, whereas the ROS quenchers such as catalase or SOD exhibited no suppression of ROS levels

(Figures 5D–5F). These studies led to the conclusion that in addition to superoxide radical anion or hydrogen peroxide, the highly reactive metal-oxo species could generate other oxidized biomolecules and promote oxidative stress. Next, we assessed the intracellular ROS generation with our lead molecules alone or in combination with oxidant (H_2O_2) and antioxidant (*N*-acetylcysteine). We used a turn-on fluorescence-based H_2DCF-DA oxidation assay in Huh-7 and U2OS cells to measure the intracellular ROS accumulation. We observed a sharp increase in the fluorescence intensity with IITK4003/4004 similar to H_2O_2 treatment, suggesting the accumulation of intracellular ROS. Conversely, combining our top hits with antioxidant *N*-acetylcysteine (NAC) has rescued the ROS effect (Figures 5G and S14). Two of the most sensitive biomolecules to intracellular ROS accumulations are deoxyribonucleic acid (DNA) and lipid molecules. First, we assessed the lipid peroxidation in cells when exposed to our lead molecules. Peroxidation of polyunsaturated fatty acids (PUFA) is known to convert them into malondialdehyde (MDA), which could be trapped using condensation chemistry with thiobarbituric acid (TBA) (Figure 5H) in a TBARS (thiobarbituric acid reactive substance) assay.[49] Quantification of MDA-TBA condensed product indicated a 2- to 3-fold enhancement in the levels of lipid peroxides (Figures 5I and S15). Besides, DNA damage is a routine mechanism predicted when metal-complex-mediated ROS generation is captured.[50] However, our analysis of H2AX protein phosphorylation at gamma position, a biomarker for DNA damage mechanism (γ-H2AX), using immunofluorescence imaging, displayed minimal or no effect compared to doxorubicin (Dox, Figures 5J and S16), thereby ruling out DNA damage mechanisms responsible for antiproliferative activity. Therefore, we concluded that the cancer cell death induced by our lead molecules could potentially arise due to lipid peroxide accumulation rather than DNA-damage-mediated mechanism.

Iron complexes accumulate lipid peroxide and do not induce ferroptosis

Thus far, the results of iron complexes enhancing intracellular ROS accumulation leading to lipid peroxidation have instinctively driven us to investigate the cell death mechanism of ferroptosis, an iron-dependent oxidative cell death induced through lipid peroxide accumulation.[51] Ferroptosis has been linked with multiple steps in the biosynthesis of glutathione and its redox cycling. For example, erastin is reported to inhibit cystine uptake to induce ferroptosis by targeting System Xc⁻, a cystine-glutamate antiporter system. RSL3 is a ferroptosis inducer that inhibits glutathione peroxidase 4 (GPX4), a lipid peroxidase enzyme that employs glutathione for quenching lipid peroxides and directly inhibits ferroptosis (Figure S17A). Conversely, ferrostatin-1 (Fer-1) and liproxstatin-1 (Lip-1) are specific ferroptosis inhibitors that scavenge lipid peroxides and restore GSH levels (Figure S17A). We chose to combine these ferroptosis modulators with our lead molecules to witness the effect. Initial evaluation of canonical GPX4 inhibitor RSL3 robustly inhibited the growth of Huh-7 cells with an EC_{50} of 26 nM, and its combination with either Fer-1 or Lip-1 showed a tremendous prevention effect by more than 500-fold, thereby validating the ferroptosis assay system (Figures S17C and S17D). Whereas, combining our hits (IITK4001-IITK4004) with either Fer-1 or Lip-1 did not provide any significant protective effect (Figures S17D, S17F, and S18). Further, in our assessment, neither erastin nor RSL3 potentiated the cancer cell killing (in both Huh-7 and U2OS) by IITK4001-4004 (Figures S17B, S17C, S17F, and S18), thus dismissing the possibility of a ferroptosis cell killing mechanism for IITK4001-4004. In addition, ROS-mediated cancer cell death is known to trigger necroptosis and rapid cellular damage. However, cancer cell viability analysis for our hits in combination with necrostatin-1 (necroptosis inhibitor) showed little cell death prevention (Figure S18), thereby eliminating this possibility as well.

IITK4003/4004 induces mitochondrial dysfunction

Mitochondria, the powerhouse of cells is a sensitive organelle that responds to a sudden fluctuation of redox status. Upon exposure to toxic levels of ROS, mitochondrial membrane potential (MMP) is affected, which could be measured using established TMRM (Tetramethylrhodamine methyl ester)-mitochondria imaging by the reduction in TMRM fluorescence intensity (Figures 6A, 6B, and S19). We observed a considerable decrease in the labeling of mitochondria by TMRM in both Huh-7 and U2OS cells in the conditions treated with IITK4003/4004 and hydrogen peroxide alone or in combination (Figures 6A, 6B, and S19). Identical to the H_2DCF-DA assay, the cotreatment of IITK4003 or IITK4004 with peroxides and NAC inversely correlated with their mechanism as expected (Figures 6A and 6B). In parallel, we used MitoSOX green to capture the mitochondrial ROS accumulation (Figures 6A and 6C). We used a reported ROS generator and lipid peroxidation inducer, JCHD, as a positive control (Figures 6A and 6C).[46,47] Our molecules on their own diminished the MMP and drove low levels of mitochondrial ROS accumulation; however, upon exposure to H_2O_2, a sharp increase in the overall ROS level was detected (Figures 6A and 6C). Overall, these findings suggest that IITK4003/4004 drives ROS accumulation, which could impair mitochondrial function in cancer cells. Given that our lead molecules disrupt MMP and induce ROS accumulation in cells, we chose small molecule inhibitors of ETC complexes, rotenone (complex I),[52] antimycin A (complex III),[53] and sodium azide (NaN₃, complex IV)[54] to compare and assess the effect of IITK4003/4004 on mitochondrial function in cancer cells (Figures 6D, S20A, and S20B). One of the outcomes of mitochondrial functional inhibition is the depleted ATP levels. Our quantification of ATP levels in Huh-7 cells with lead molecules and canonical ETC inhibitors exhibited a profound decrease in ATP, assuring a parallel mitochondrial functional inhibition mechanism for IITK4003/4004 (Figures 6D and S20). Having established oxidative mitochondrial dysfunction in cells with our lead molecules, we set out to evaluate the effect of ROS modulators on the toxicity of IITK4003/4004 to Huh-7 cells. Therefore, we combined buthionine sulfoximine (BSO, a glutathione biosynthesis inhibitor, induces oxidative stress) and antioxidants (vitamin E [Vit-E] and NAC) with IITK4001-IITK4004 independently, to capture their effect on the proliferation of cancer cells (Figures 6E, 6F, and S21). We observed a uniform trend of dose-dependent enhancement of cell death with BSO and a protective effect by Vit-E/NAC for all the molecules tested (Figures 6E and 6F). This is effectively suggesting oxidative stress induction is a relevant molecular mechanism of our lead molecules.
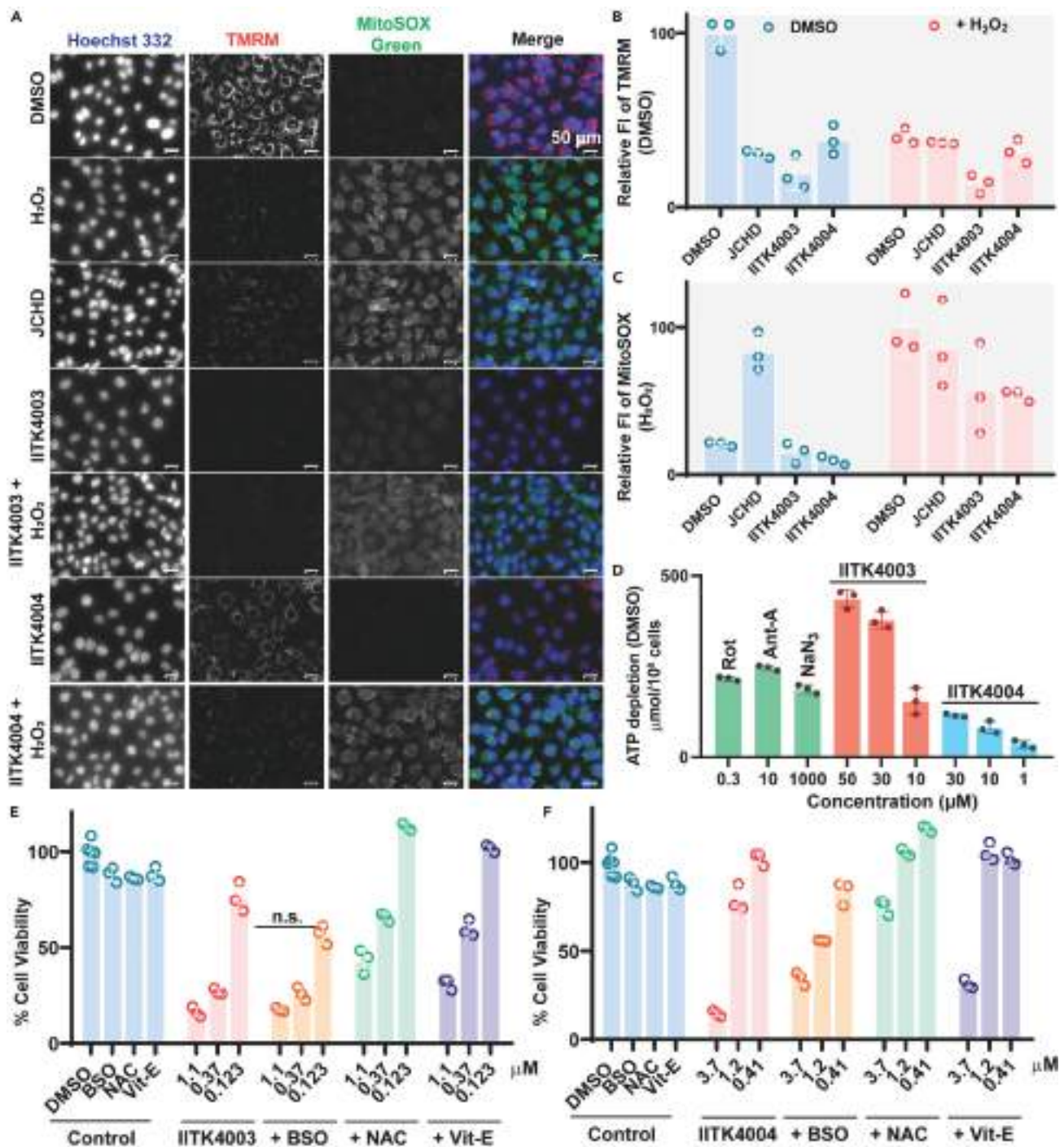
Figure 6. IITK4003/IITK4004-induced ROS accumulation led to mitochondrial dysfunction and correlated with ROS-mediated Huh-7 cell death

(A–C) Effect of indicated compounds and combinations on MMP in Huh-7 cells imaged using a potentiometric fluorophore, TMRM, and ROS accumulation with MitoSOX Green using fluorescence microscopy (A) and their relative fluorescence intensity quantified data (B, C). Scale bar: 25 μm.

(D) Reduction in the levels of ATP quantified using a luminescence-based Celltiter-Glo assay in Huh-7 cells upon treatment with indicated molecules.

(E and F) Effect of additional non-toxic dose of oxidants (BSO-50 μM) and antioxidant (Vit-E-300 μM, NAC-500 μM) on the cell viability of Huh-7 cells treated with IITK4003 (E) or IITK4004 (F) at indicated concentrations. Graphs B–F indicate mean ± SD. Data presented are representative of more than two independent replicates and a minimum of three technical replicates. Cell viability data are normalized relative to DMSO treatment control as 100%.

IITK4003/4004 trigger caspase cascade to induce apoptosis

Oxidative mitochondrial impairment leads to the release of mitochondrial proteins including cytochrome c into the cytosol, which are known to activate caspase cascade and trigger apoptosis.[55–57] Therefore, we used multiple sets of experiments including combination treatment cell viability studies, immunoblotting, and immunofluorescence imaging to capture the cell death mechanism (Figure 7). First, we investigated the effect of apoptosis, a programmed cell death inhibitor, QVD-OPh (a pan-caspase inhibitor), in combination with our lead molecules in Huh-7 and U2OS cells (Figures 7A and S23).[58,59] We observed profound rescue of cell death by QVD-OPh when combined with lead molecules, thereby hinting a likely apoptosis mechanism (Figure 7A).[60] Then, we conducted immunofluorescence imaging to visualize the apoptosis biomarkers in the cells treated with our molecules. We stained the cells for annexin-V (an apoptosis biomarker) and propidium iodide (PI, for tracking cell death) after treatment with our molecules (Figures 7B, 7C, S24, and S25). We found a remarkable increase in the staining for annexin-V and PI in cells treated with our molecules, and a cotreatment with QVD-OPh rescued the PI staining (Figures 7B, 7C, S24, and S25). Next, we performed immunoblotting for tracking the activation profiles of caspase-cascade-mediated apoptosis markers. First, we confirmed the release of mitochondrial cytochrome c (Cyt c) to the cytoplasm after treatment with our lead molecules and the positive control (Figure 7D). We observed a comparable effect on the release of cytochrome c for both the ligands as well as the complexes' treatment (IITK4001-IITK4004). Then, a time-dependent (4 h and 8 h) analysis of full-length caspase-3 and its activation to release cleaved caspase-3 indicated a sharp increase in the caspase-3 activation over time, and this was comparable to the positive control, staurosporine (Figures 7E, 7F, and S26). The subsequent effect of caspase-3 activation to trigger the cleavage of death substrate poly [ADP-ribose] polymerase 1 (PARP-1) exhibited a strong correlation with our lead-molecule-mediated apoptosis in two independent cell lines (Figures 7E, 7F, and S26). Interestingly, both the ligands (IITK4001 and IITK4002) were found to exert strong effect on the caspase-3 cleavage when compared to their respective complexes (Figures 7E and S26), which was comparable to that of positive control staurosporine in Huh-7 cells, and effect was found to be extending to PARP-1 cleavage. Whereas in U2OS cell line, we have observed a stronger band for cleaved caspase-3 and PARP-1 for the complex 4004 over the ligand IITK4002. Despite the relatively slight difference on the extent of caspase-cascade activation, both ligand and complexes were highly effective in preventing the cancer cell growth and induced apoptosis (Figures S7 and S22–S26). Collectively, the abovementioned set of experiments strongly suggests that our lead molecules induce mitochondrial dysfunction and released Cyt c into the cytoplasm to trigger the caspase cascade that promoted the intrinsic apoptotic cell death mechanism in cancer cells.

Pan-cancer activity and 3D-spheroid growth inhibition by IITK4003/4004

Further, to emphasize the generality of IITK4003/IITK4004 to act as proliferation inhibitor of various cancer phenotypes, we have screened the indicated molecules against a panel of 10 more cancer phenotypes in addition to Huh-7 and U2OS (Table 1, Figure S27). We observed growth inhibition of cancer cells within a range of 0.3–3.5 μM EC_{50} against all the cancer lines investigated. We found Huh-7 cells to be highly sensitive to IITK4003 with an EC_{50} at 340 nM concentration, whereas other cancer phenotypes exhibited comparable sensitivity. Among the hepatocellular carcinoma (HCC) cells, the sensitivity of Huh-7 cells was nearly 10-fold higher than HepG2 cells (Table 1, Figure S27). These drastic differences in selectivity could be attributed to several factors including genetic and metabolic differences and higher lipogenesis in Huh-7 cells over other hepatoma cells,[61–63] which is an interesting lead for future explorations. In the case of IITK4004, the molecules exhibited comparable cell-killing potency (2.2–3.5 μM) with all the cancer cell lines tested (Table 1, Figure S27). Extending the studies to 3D-cell models such as spheroids will help us capture the ability of our molecules to penetrate the tissue-like structure and inhibit their growth. Therefore, we have generated 3D-spheroids of HepG2 cells and treated them with mitomycin as a positive control to establish a functional assay system. Then the treatment of spheroids with IITK4003 and IITK4004 showed an excellent reduction in the scaffold size of spheroids in a dose-dependent fashion (Figures 8A–8C). These results together highlight that these molecules can prevent multiple cancer phenotypes and they can be successful in inhibiting tumor growth *in vivo* as indicated by volume reduction in the prototype, 3D-spheroids.

Nanocarrier potentiating the activity of IITK4003/4004 in liver cancer cells

Our studies for IITK4003 in multiple cancer phenotypes showed a variable EC_{50} (0.34–3.3 μM, a 10-fold difference), whereas a comparable EC_{50} was recorded for IITK4004 (2.2–3.9 μM) in all the cell lines investigated (Table 1, Figure S26). At higher concentrations, we found aqueous solubility issues for IITK4003 over IITK4004; therefore, it was suspected that the differential EC_{50} in various cell lines could be an outcome of differential cell permeability. Hence, to evaluate this possibility, we have performed inductively coupled plasma resonance mass spectrometry (ICP-MS) and energy dispersive X-ray spectroscopy and scanning electron microscopy (EDX-SEM) of HUH-7 cell treated with DMOS or lead metal complexes (20 μM, Figures S28 and S29). We have observed a distinct increase in the iron levels in both ICP-MS and EDX-SEM analysis in the metal-complex-treated conditions. Indeed, under comparable conditions, the iron level was quantified to be slightly higher in the case of IITK4004 over IITK4003, thereby reflecting on the differential aqueous solubility impacting cell permeability of the complexes. Therefore, to improve the local concentration of the metal complexes intracellularly, a polymeric nanosized drug carrier was synthesized for the effective delivery of IITK4003 and IITK4004, which would overcome the problem associated with water solubility and cell permeability. A water-in-oil-in-water emulsion method (Scheme S3) was employed for the preparation of the nanocarriers (NCs) using an amphiphilic, diblock amphiphilic copolymer carboxylic acid poly (ethylene glycol)-block-poly(lactide-co-glycolide) (PLGA-b-PEG-COOH). The molecules of interest, IITK4003 and IITK4004, were added to the polymer solution at the first step of preparation of NCs, which led to an effective entrapment of molecules, presumably inside the hydrophobic core of the nanocarriers (Scheme S4). Dynamic-light-scattering-based investigation revealed that the effective hydrodynamic diameter of synthesized NCs was 186 ± 2.5 nm. It was noticed that there was no significant change in effective
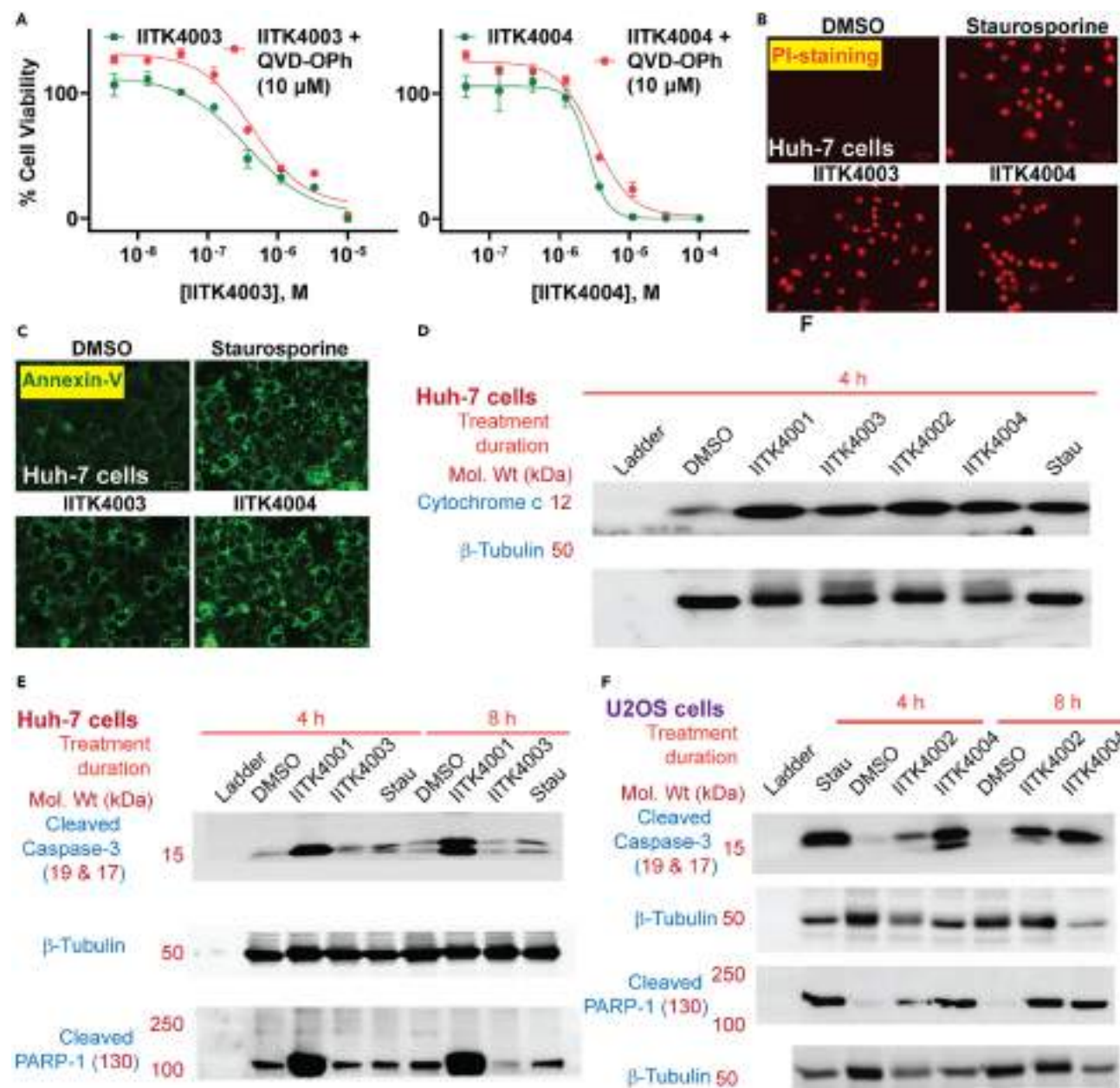
Figure 7. IITK4003/IITK4004 triggers the caspase cascade to promote apoptosis in cancer cells

(A) Cell viability studies of Huh-cells upon cotreatment of apoptosis inhibitor QVD-OPh (10 μM, A) with our lead molecules.

(B and C) Induction of apoptosis in Huh-7 (E) and U2OS (F) cells by IITK4001/4003 (20 μM) and staurosporine (250 nM) was captured using a fluorescence imaging of propidium iodide (PI)-stained nuclei and immunostaining for an apoptosis marker, Annexin-V.

(D–F) Immunoblotting for indicated apoptosis markers in Huh-7 (D, E) and U2OS cells (F) after 4 h and 8 h of treatment with IITK4001-IITK4004 (30 μm) and the positive control staurosporine (100 nm). Protein concentration in each lane was 20 μg; all molecules were used at 30 μM, except Stau: staurosporine, 100 nM). Graphs A–D indicate mean ± SD. Data presented are performed in two independent cell lines and are representative of more than two independent experiments with a minimum of three technical replicates. Cell viability data are normalized relative to DMSO treatment control as 100%.

hydrodynamic diameter of NCs on loading of the IITK4003 and IITK4004 in nanocarriers, called as NC/IITK4003 and NC/IITK4004, respectively (Figures 9A and S30). The effective hydrodynamic diameter of NC/IITK4003 and NC/IITK4004 was 184 ± 1.5 nm and 183 ± 7.5 nm, respectively. The polydispersity index (PDI) values of NCs, NC/IITK4003 and NC/IITK4004 nanosuspension, were found to be 0.18 ± 0.01, 0.14 ± 0.01 and 0.23 ± 0.02, respectively (Figure 9B). These low PDI values implied the homogeneous nature of the polymeric nanocarriers, which was retained even after loading IITK4003 and IITK4004. This observation was also supported by the intensity vs. size distribution plot as

Table 1. Cell viability analysis of various cancer cell lines with IITK4003 and IITK4004 (EC$_{50}$ values with an average SD of ± 0.1 μM for IITK4003 in Huh-7)

Cancer cell line	IITK4003 (μM)	IITK4004 (μM)
Huh-7	0.34	2.2
Huh-7[a]	0.11	1.9
HepG2	4.87	3.07
HepG2[a]	0.42	2.8
HEK293	3.82	7.6
A549	1.99	2.3
Jurkat-6	1.6	2.2
MCF7	1.41	2.7
MDA-MB-231	2.1	2.4
U2OS	2.10	2.3
A375	ND	2.9
HCT116	ND	2.6
PC3	ND	3.5
RPMI 8226	ND	2.3
U87MG	ND	4.0

[a]EC$_{50}$ of the IITK4003/IITK4004 encapsulated in nanocarrier; N.d., not determined. Cancer cell lines: A549: lung carcinoma epithelial cells; HepG2 & Huh-7: hepatocellular carcinoma; Jurkat J6: acute T-cell leukemia; MCF7: breast cancer MDA-MB-231; triple negative breast cancer; U2OS, osteosarcoma; A375, melanoma; HCT-116, colon cancer; PC3, prostate cancer; RPMI 8226, B lymphocytes; U87MG, glioblastoma.

represented in Figure 8C for NCs and NC/IITK4003, NC/IITK4004, and their imaging (Figure 9D). Further, the loaded amount of IITK4003 and IITK4004 was quantified by analyzing the absorbance vs. concentration standard plot. It was found that the loaded concentration of IITK4003 and IITK4004 in NCs was 34.8 and 194 μM, respectively (Figures 9E and 9F). This quantification deciphered that the entrapment of two water insoluble molecules, IITK4003 and IITK4004, inside polymeric NCs brought these molecules into aqueous suspension in significantly higher concentration and eventually be available to the biological system for uptake possibly through endocytosis.[64–66] These lead-molecule-encapsulated nanocarriers were evaluated in both Huh-7 and HepG2 cells for their antiproliferative activity. NC/IITK4003 exhibited nearly a 4-fold (0.43–0.11 μM) in Huh-7 and 12-fold (4.87–0.42 μM) enhancement in EC$_{50}$ HepG2 cells (Figures 9G–9K). Under comparable conditions, we found no significant difference in the EC$_{50}$ for IITK4004 between the pristine treatment or nano-encapsulated form NC/IITK4004. Collectively, our effort to enhance the effective delivery of IITK4003 through nanoencapsulation resulted in the identification of exceptionally potent growth inhibition of Huh-7 cells at 110 nM EC$_{50}$.

DISCUSSION

Drug resistance in cancer is a serious global threat, and identification of novel therapeutic interventions is a high priority. Emerging technologies including PROTACs (small-molecules-based proteolysis activating chimeras for target protein degradation), CRISPR-Cas systems (for genetic manipulations), and antibody-drug conjugates offer promises. In parallel, classical drug discovery approaches using small molecules to target specific disease-relevant proteins and/or cellular functional machinery have also continued to evolve. Cisplatin set the foundation for metal-based therapeutics, and it was approved nearly five decades ago by US-FDA (1978) for cancer treatment. Since then, only fewer metal complexes entered clinical trials, and overall metal-complex-based cancer therapeutics development remains underdeveloped. Recently, modulation of intracellular metal ion levels to alter redox homeostasis is emerging as a potential therapeutic modality to prevent cancer progression.[25,26] Targeting this redox sensitivity, several ruthenium-based compounds with systematically varied ligands core have been developed as potential anticancer therapies.[10–12,67–75] Moreover, iron complexes of ferrocene, salen, and N-heterocyclic ligands are developed as potential anticancer agents, exerting their effects by triggering reactive oxygen species (ROS) production within cancerous cells at micromolar concentrations.[13–16] We identified IITK4001 and IITK4002 as a potential candidate for promoting apoptosis in cancer cells at 110 nM potency. We provided a comprehensive understanding of IITK4001/4002 as trapping intracellular iron by complexation and ROS-mediated mitochondrial function impairment to promote apoptosis in cells (Figure 10). Interestingly, there is no literature evidence of the characterization of reactive iron oxo species generated by IITK4004 in water, possibly owing to the challenge associated with their poor stability in aqueous milieu. However, high-valent reactive metal oxo species in organic solvents and their utility in catalysis such as oxygen atom transfer reactions are known.[39] One of the key aspects is we have successfully characterized the short-lived high-valent Fe(IV)=O intermediates in water to set the literature precedence. Notably, IITK4003/4004-mediated ROS generation and accumulation of lipid peroxide did not trigger ferroptosis. Perhaps, the concentration of lipid peroxide accumulation induced by our molecules is not sufficient to trigger ferroptosis, which is also reflected in the absence of necroptotic cell death (typically activated with excess ROS).[76,77] Mitochondrial components such as cytochrome c released into cytoplasm leading to the activation of caspase cascade to trigger apoptosis augurs well with our mechanism since our
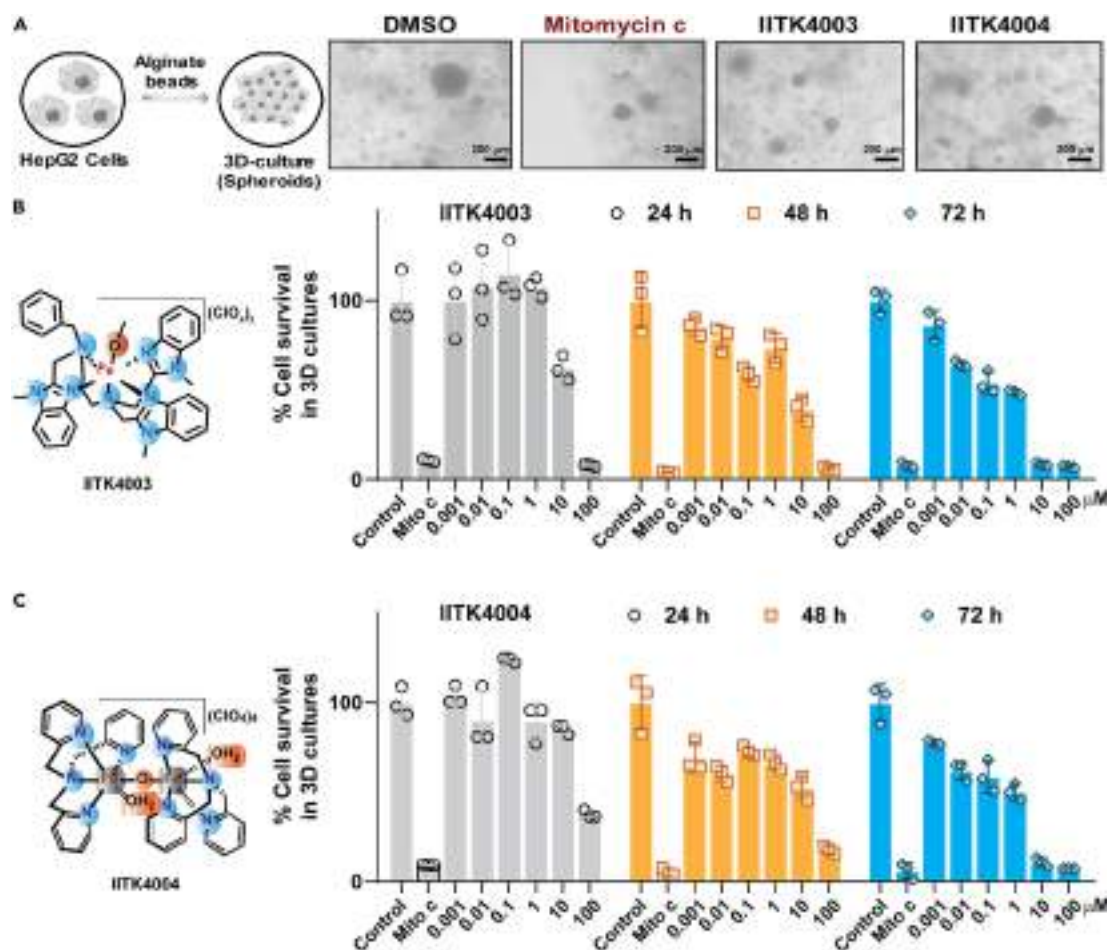
Figure 8. Our lead molecules IITK4003/IITK4004 reduced the 3D-spheroid volume and dose-dependently inhibited their growth
(A) Schematic and images of HepG2 cells spheroids generated out of 3D-culture and their treatment with indicated molecules after 72 h. Scale bar: 200 μm.
(B and C) 3D-culture cell viability was assessed during their treatment with IITK4003/IITK4004 for 24, 48, and 72 h using MTT assay. Graphs B and C indicate mean ± SD. Data presented in (A–C) are representative of two or more independent experiments with a minimum of three technical replicates. Cell viability data are normalized relative to DMSO treatment control as 100%.

lead molecules were found to promote mitochondrial dysfunction. Though we obtained an excellent EC_{50} for IITK4003 in Huh-7 cells and were good at reducing the size of HepG2-spheroids, we observed solubility issues at higher concentrations. Initially, we suspected the solubility and cell permeability could potentially dictate the EC_{50} of IITK4003 in various cell lines. A head-to-head comparison of IITK4003 and its nano-encapsulated version NC/IITK4003 in both Huh-7 and HepG2 exhibited a remarkable improvement in the overall potency indeed confirming the effective delivery of IITK4003 could be a serious contributor to improve the efficiency of the molecules. In summary, our study suggests that an angle of metal trapping and subsequent chemical reactivity and improvisation of local drug concentration could be used for heterocyclic molecules' biological activity and to study their mechanism of action.

Limitation of the study

We report that nitrogen-based heterocyclic scaffolds form complexes with iron to induce antiproliferative activity in cancer cells. The proposal was established by synthesizing authentic iron complexes and evaluating them for their antiproliferative activity and their mechanism of action studies. However, proving the complexation with intracellular iron was not possible due to minute change in the intracellular iron concentration with IITK4002 addition (our ligands are active in low micromolar concentrations and cellular iron levels ~20 μM). This could be addressed by synthesizing structurally close turn-on fluorescent probes for intracellular iron, which is a scope for future research. Further, though the biological activity of IITK4001 was mimicked in the respective iron complex, IITK4003's outstanding response in cells could not be studied as the solubility issues associated with IITK4001 under physiological conditions have hampered our plans of establishing iron complexation mechanism inside cell. Additional modifications in the structure to enhance the solubility of IITK4001 to improve the potency and to decipher the mechanism of action is another direction to pursue. Future experiments could include ICP-MS analysis of HEK293 cells treated with lead

RESEARCH ARTICLE
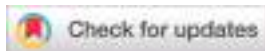
Check for updates

A Cu(II) pseudopeptide complex: a surrogate to a *formal* Cu(III) species in water and an inhibitor of cancer cell proliferation†

Raju Eerlapally,[a] Sai Kumari Vechalapu,[a] Santosh Duraisamy,[a] Divya Lakshmi Hareendran,[a] Jayashrita Debnath, [iD] *[b] Dharmaraja Allimuthu [iD] *[a] and Apparao Draksharapu [iD] *[a]

Metalloenzymes play a crucial role in life, performing myriad functions in aqueous environments in nature. Understanding these systems' structural and functional mimics in water at ambient temperature is essential for developing new catalysts. Inspired by nature, we report here the synthesis of a remarkably stable *formal* [(L)Cu(III)]⁺ (**2**) species supported by a tetradentate pseudopeptide ligand, which we then characterized by various spectroscopic techniques in water at ambient temperature and using DFT methods. Our experimental and DFT studies indicate that the observed stability is caused by hydrogen bonding of water molecules to the amide moiety of the ligand bound to the *formal* Cu(III) center. The Natural Bonding Orbital (NBO) analysis indicated the best description of the oxidized species to be *formal* Cu(III). The *formal* Cu(III) species (**2**) could also be prepared by electrochemical oxidation methods in water. The generated species **2** was found to be reactive towards various phenols in $H_2O : CH_3CN$ (1 : 1). The ability to stabilize *formal* Cu(III) in water encouraged us to investigate the biological activity of [(L)Cu (II)] (**1**) in cancer cell proliferation. Studies of these metalloenzyme mimics in cells indicated that intracellular and extracellular reactive oxygen species (ROS) generation, in turn, selectively prevented the growth of liver cancer cells over other cancer cell lines and normal kidney cells.

Introduction

Copper-containing proteins are prevalent in biological systems and play an essential role in O_2 activation, C–H activation, and electron transfer reactions.[1–3] One such enzyme is peptidylglycine alpha-hydroxylating monooxygenase (PHM), which hydroxylates the C_α of a C-terminal glycine. The other well-characterized enzyme related to PHM is dopamine β monooxygenase (DβM) in the human brain, accountable for the biosynthesis of adrenaline by converting dopamine to norepinephrine.[4,5] There is another class of enzymes called lytic polysaccharide monooxygenases (LPMO), which plays an essential role in the depolymerization of sugar-based biopolymers (cellulose, hemicellulose, chitin, and starch) and has a positive impact on biomass conversion.[6,7] The oxidation state

of copper shuttles between +1 and +2. However, the Cu(III) species is also proposed to be one of the active intermediates in the catalytic cycle. Nonetheless, direct spectroscopic evidence for the Cu(III) species in biological systems is scarce thus far, to the best of our knowledge.[8,9] Cu(III) has also been proposed to be used in Cu-assisted synthetic transformation reactions like formation of carbon–carbon bonds and carbon–heteroatom bonds in Cu-catalyzed cross-coupling reactions.[10,11] Understanding the structure and reactivity relationship of such transient species is critical for obtaining mechanistic insight into oxidation catalysis.

Various groups across the globe have been working to develop synthetic models for transient Cu(III) intermediates. These include Tolman's Cu(III)–OH with a dianionic N3 donor ligand,[12] Garcia-Bosch's *formal* Cu(III)–OH complex of a dianionic N3 ligand,[13] Bernhardt's Cu(III) with bis-dithiocarbazate,[14] Llobet's Cu(III) complex having a macrocycle as a supportive ligand,[15] Meyer's Cu(III) complex with a bispyridine-biscarbene ligand and a macrocyclic ligand framework,[16–18] Kruger's Cu(III) complex with a bisamido-bisthiolate framework,[19] Collins and Paria's Cu(III) complex with a bisamido-bisalkoxy ligand framework[20,21] and Draksharapu's Cu(III) complex supported by a proline based pseudo peptide[22] to name a few (Fig. 1).

[a]Southern Laboratories, Department of Chemistry, Indian Institute of Technology Kanpur, Kanpur-208016, India. E-mail: appud@iitk.ac.in, atdharma@iitk.ac.in
[b]Department of Theoretical Biophysics, Max Planck Institute of Biophysics, Frankfurt am Main, Germany. E-mail: jayashritad@gmail.com
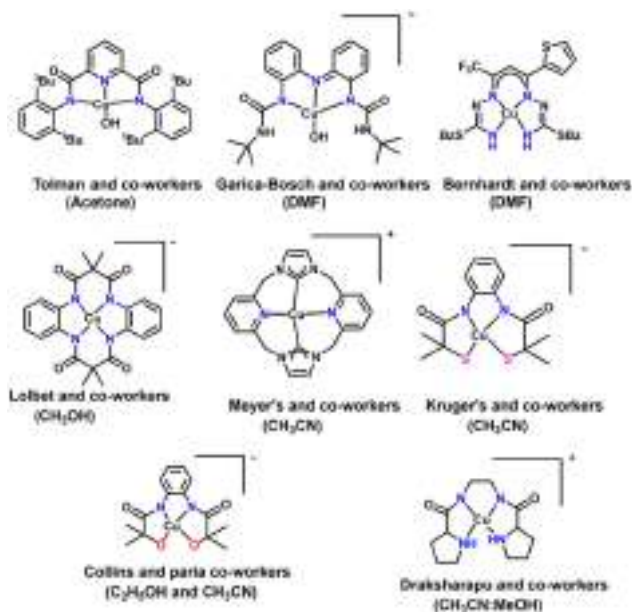
Fig. 1 The reported structurally characterized high valent Cu(III) complexes in various solvents.

According to a thorough literature survey, it was observed that electronically rich ligands with amides and alkoxy moieties can stabilize high valent copper species effectively. Furthermore, due to their inherent instability, most Cu(III) intermediates were characterized at lower temperatures in various organic solvents. However, natural enzymes utilize water as a medium for functional activity at ambient temperatures, which impacts enzymatic catalysis through hydrogen bonding interactions.[23] Therefore, characterizing these intermediates in water is significantly relevant to biology. Here, we have investigated the formation of a *formal* (L)Cu(III) (**2**) intermediate from the reaction of (L)Cu(II) (**1**, LH$_2$ = *N,N'*-(ethane-1,2-diyl)bis(pyrrolidine-2-carboxamide)) with *m*CPBA in water at 25 °C (Fig. 2) and characterized it extensively using various spectroscopic studies such as UV/Vis absorption, electron paramagnetic resonance (EPR), resonance Raman, X-ray photoelectron spectroscopy (XPS) and ESI-MS. DFT calculations supported our experimental observations. The hydrogen bonding interaction of water with the amide oxygen of the ligand bound to the copper centre makes it stable in water. The intermediate **2** described in the present study can perform hydrogen atom abstraction (HAA) from phenol and its derivatives. The fact that we can stabilize a *formal* Cu(III) in water inspired us to explore the biological activity of **1** in cancer cell prolifer-

ation. To our delight, **1** enhanced the cellular ROS and promoted mitochondrial functional impairment in cancer cells. The enhanced oxidative environment inhibited the growth of liver cancer cells selectively over that of normal kidney cells, with a >17 selectivity index.

Results and discussion

Our previous study reported the synthesis and spectroscopic characterization of the (L)Cu(II) complex, **1**. Treatment of **1** with *m*CPBA in MeOH : CH$_3$CN (1 : 20) at −30 °C gave rise to an absorption band at 430 nm. This 430 nm absorbing species was assigned to the *formal* [(L)Cu(III)]$^+$ (**2**) species supported by various spectroscopic techniques like EPR, resonance Raman (rR), ^{1}H NMR, and ESI-MS analyses.[22] In the present work, we explored the possibility of generating the high valent *formal* [(L)Cu(III)]$^+$ species in water and characterized it with different spectroscopic techniques and computational methods.

Electrochemical studies of **1** were carried out in water to learn about its redox properties. **1** exhibits a reversible Cu(III)/Cu(II) redox wave with $E_{1/2}$ = 0.55 V *vs.* Ag/AgCl (Fig. 3B and S1†).[22,24] This value is comparable to the redox potential observed in a MeOH : CH$_3$CN (1 : 20) solvent system. The reversible behaviour of the cyclic voltammogram supports our hypothesis of the possible formation of Cu(III) in water. The almost similar value of the potential for the Cu(III)/Cu(II) redox couple both in water and MeOH : CH$_3$CN (1 : 20) mixture suggests that axial binding of the solvent as a ligand does not take place upon dissolution (Fig. 3 and S1†). This notion is supported by the ESI-MS analysis of **1** in water, which revealed a signal at *m/z* 316.0956 that can be formulated as [LCu(II)]H$^+$ (Fig. S2†).

The ligand contains two basic amide moieties, which may cause the complex to become pH-sensitive in terms of Cu(II) coordination. The pH-dependent studies on (L)Cu(II) **1**, with an initial pH of 8.51, were performed by incremental addition of HClO$_4$ (up to 3 equivalents). A gradual redshift in 504 nm to 580 nm absorption was observed when the pH reached 5.76 (Fig. S3†). Further addition of acid causes the decay of the 580 nm species. Treatment of the 580 nm species with 3 eq. of KOH reverts **1**. The 580 nm species is identical to a dimeric species, [(LH$_2$)$_2$Cu(II)$_2$]$^{2+}$, which is crystallographically charac-

Fig. 2 Strategies described in the current work for the formation of *formal* (L)Cu(III) in water at 25 °C.
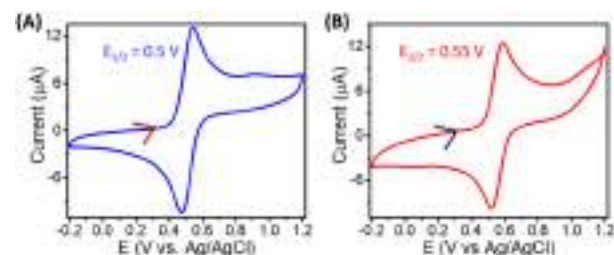

Fig. 3 Cyclic voltammograms of **1** (1 mM) (A) in MeOH : CH$_3$CN (1 : 20) and (B) H$_2$O at a 100 mV s^{-1} scan rate.

terized (Fig. S4 and Table S1†).[18,25] Furthermore, this dimeric species was characterized by UV/Vis absorption spectroscopy, which showed an absorption at 598 nm ($\varepsilon_{598\ nm}$ = 70 M^{-1} cm^{-1}), corresponding to d–d transitions (Fig. S5†). EPR analysis of this dimeric species revealed an isotropic signal with a g value of 2.12, indicating that copper is in the +2 oxidation state, with the two copper centers not communicating with each other (Fig. S6†).

The reaction of **1** with 1 eq. of mCPBA in phosphate buffer (pH 8) generated a weak absorption band at 410 nm (Fig. S7†). However, the same reaction in non-buffered water gave rise to a yellow-colored species with a stronger absorption band at 410 nm ($\varepsilon_{410\ nm}$ = 1280 M^{-1} cm^{-1}) and 25 °C (Fig. 4A). The addition of different eq. of mCPBA to **1** suggests that the formation rate of **2** depends on the concentration of mCPBA. The maximum yield of **2** was obtained with 1 eq. of mCPBA. In the presence of excess mCPBA, the yield and stability of **2** decrease significantly (Fig. S8†).[26] It has been observed that changing the solvent from MeOH : CH$_3$CN (1 : 20) to H$_2$O enhances the

stability of **2** and shows a blue shift of 25 nm in the absorption band (Fig. 4B). Additionally, we also generated **2** at 37 °C as this temperature is relevant to physiological conditions (Fig. S9†). Furthermore, we performed UV-Vis analysis in H$_2$O : CH$_3$CN (1 : 1) to facilitate the reactivity studies with phenolic substrates (*vide infra*). In this case, treating **1** with 1 eq. of mCPBA gave a band at 414 nm. A slight shift from 410 nm is probably due to the solvatochromic effect (Fig. S10†). However, the stability of the intermediate is not affected upon introducing CH$_3$CN to the solvent system.

To probe the oxidation state of the generated intermediate **2** we employed EPR spectroscopy by acquiring EPR spectra at various time intervals. The initial (L)Cu(II) shows an isotropic signal with a g value ~2.08, suggesting one unpaired electron in the system, *i.e.*, $S = \frac{1}{2}$ Cu(II) species (Fig. S11†). The usual axial signal for Cu(II) complexes is not observed in the current case, probably due to increased electron spin–lattice relaxation and considerable exchange coupling.[27] However, we observed an axial signal for Cu(II) in MeOH : CH$_3$CN (1 : 20) in our previous studies. It has been observed that during the reaction, the intensity of the Cu(II) signal decreases over time. The maximum signal intensity loss was observed at 35 s, indicating the conversion from Cu(II) to a diamagnetic species (Fig. 5A). The EPR spin quantification at the maximum accumulation of the intermediate revealed that a 52% $S = \frac{1}{2}$ Cu(II) signal is present in the solution. The remaining 48% EPR silent 414 nm species can be ascribed to a diamagnetic species. However, the EPR silent nature of species **2** (Fig. 5A) can also be ascribed to a possible dimeric species. To verify the possibility of forming dimeric species, concentration-dependent kinetic experiments for the formation of **2** were performed on (L)Cu(II) (**1**). The plot of k_{obs} *vs.* [**1**] was fit through linear regression, resulting in good linear dependence, which indicates first-order rate kinetics with respect to **1** (Fig. 5B). These data demonstrate that in the rate-determining step, only one copper center is involved
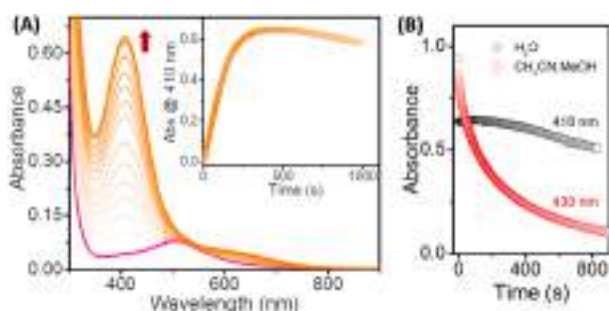

Fig. 4 (A) UV/Vis absorption changes upon addition of 1 eq. of mCPBA to 0.5 mM **1** in water at 25 °C. (B) Stability comparison of **2** in MeOH : CH$_3$CN (1 : 20) (red trace) and **2** in H$_2$O (black trace) at 25 °C. Note: The path length of the cuvette used is 1 cm.
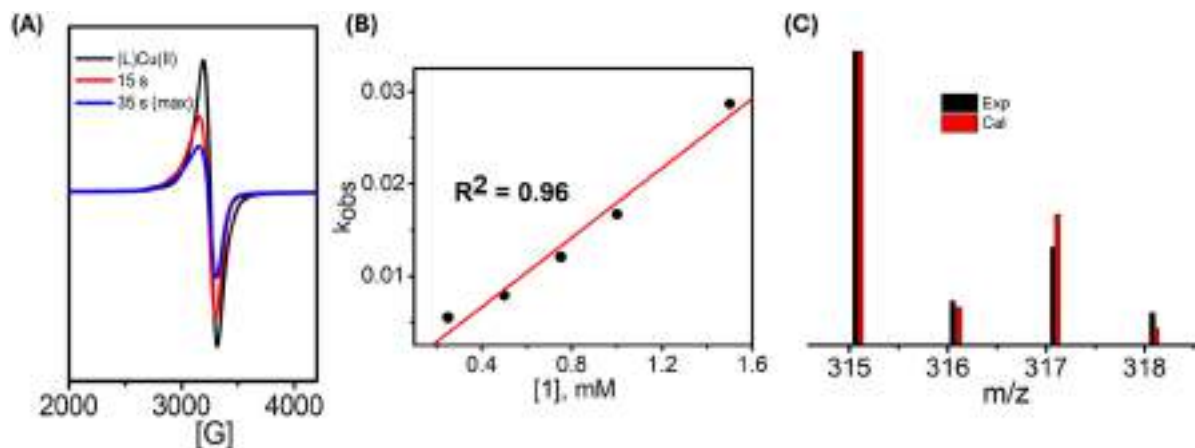

Fig. 5 (A) Formation of **2**, followed by X-band (frequency = 9.432 GHz) EPR spectroscopy at various time intervals as mentioned in the legend at 120 K; modulation amplitude: 1.98 G; modulation frequency: 100 kHz, and attenuation: 18 dB. Conditions to generate **2**: 2 mM **1** in H$_2$O : CH$_3$CN (1 : 1) + 1 eq. of mCPBA at 25 °C. (B) Linear dependence on [**1**] of the formation rate of **2** at 25 °C. (C) ESI-MS data for **2** in H$_2$O : CH$_3$CN (1 : 1) at room temperature (black) experimentally obtained data (red) and simulated data.

and excludes the possibility of dimeric species in the solution. Furthermore, ESI-MS analysis of **2** shows a major signal at an m/z value of 315.0866, which can be formulated as $[(L)Cu(III)]^+$ (Fig. 5C and S13†). Further ^1H NMR analysis of **2** reveals a signal in the diamagnetic region which indicates that copper is in its *formal* +3 oxidation state (Fig. S14†). To differentiate between ligand and metal center oxidation, we utilized X-ray photoelectron spectroscopy (XPS). The stability of compound **2** allowed us to isolate it as a solid for XPS analysis. The Cu 2p XPS data of **2** exhibited two peaks at binding energies of 934.60 eV (Cu $2p_{3/2}$) and 954.36 eV (Cu $2p_{1/2}$) (Fig. S15†). The observed signal at 934.60 eV falls within the range associated with known Cu(III) $2p_{3/2}$ signals.[28,29] Furthermore, the Cu 2p XPS data of compound **1** revealed two peaks at binding energies of 933.30 eV (Cu $2p_{3/2}$) and 953.20 eV (Cu $2p_{1/2}$), which are typical of Cu(II) complexes. The difference in binding energy of the Cu $2p_{3/2}$ signal between **1** and **2** is 1.3 eV, indicating more oxidizing nature of copper in **2**. Together, these studies support the formulation of **2** to be a *formal* Cu(III) species. To investigate the identity of 410 nm, **2** was subjected to resonance Raman spectroscopy. The resonance Raman spectrum acquired at the maximum formation of 410 nm species displayed multiple resonantly enhanced bands at 1614, 1442, 1102, 1037, 867, 609, and 431 cm^{-1} (Fig. 6) which are considered to arise from ligand vibrations. Notably, all these bands vanish in the decayed sample. It is noted that the stretching frequency of the amide functional group, *i.e.*, 1614 cm^{-1}, is derived from C=O stretch. However, species **2** generated in the MeOH : CH$_3$CN system exhibited a C=O stretch at 1648 cm^{-1} instead.[22] The shift of −34 cm^{-1} in water can be ascribed to the hydrogen bonding interaction of water with the basic amide oxygen of the ligand framework, which is absent in acetonitrile. This is also in line with the observed shift of 25 nm in the UV/Vis absorption spectrum of **2** in water

(*vide supra*). In the present case the carbonyl stretching frequency is 1592 cm^{-1} for Cu(II), whereas for **2**, it is 1614 cm^{-1}.

The findings of cyclovoltammetry make it amply clear that the Cu(III) oxidation state in water can be accomplished without any axial ligation. To verify that the electrochemically generated species is the same as the chemically generated **2**, we performed spectroelectrochemical oxidation of **1**. The electrochemical oxidation of **1** in water at an applied potential of 0.6 V *vs.* Ag/AgCl generated an absorption band at 410 nm (Fig. S12†). This 410 nm band is virtually the same as that of the species generated through the chemical oxidation of **1** with *m*CPBA in water. It is concluded that the spectroelectrochemically and chemically generated species **2** is a *formal* Cu(III) species (*vide infra*).

Computational studies

We used TD-DFT to calculate the UV-Vis spectra for the optimized minimum energy structures. In the ESI,† we have compared the spectra of **2** in CH$_3$CN, **2** in water, **2**·2H$_2$O in water. We found that the spectra for **2** are almost indistinguishable, irrespective of the solvent used. However, we could observe a blue shift when two water molecules are hydrogen bonded to **2**. This is consistent with the experimentally observed redshift in the absorption band in water compared to that in acetonitrile. In addition to UV-Vis spectra (Fig. S16†), we have also compared the theoretically calculated Raman frequencies for these three systems. We observed that the frequencies for **2** in CH$_3$CN and water were very similar. However, the carbonyl stretching frequency for **2**·2H$_2$O in water shifted towards a lower value (Fig. S17 and S18†). Therefore, our theoretical and experimental findings are consistent with each other. All our results indicate that **2** behaves similarly irrespective of the solvent used, and it is only when water is hydrogen bonded to the carbonyl groups that we can see significant changes in its behaviour.

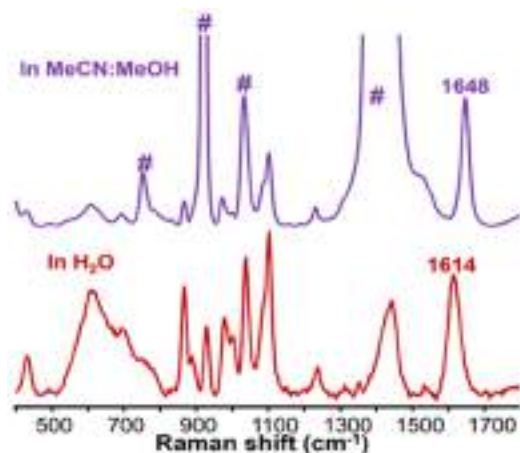We optimized the complex **2** with a variable number of hydrogen-bonded water molecules. From Fig. 7 and Table S2,†

Fig. 6 Resonance Raman spectra (λ_{ex} = 457 nm) of **2** acquired at the maximum accumulation of the 410 nm band (**2**) generated by reacting 2.2 mM **1** with 1 eq. of *m*CPBA in water at RT (violet) and its comparison with the *formal* (L)Cu(III) generated in MeOH : CH$_3$CN (1 : 20) at −30 °C (maroon).[18] #Indicates solvent derived bands.
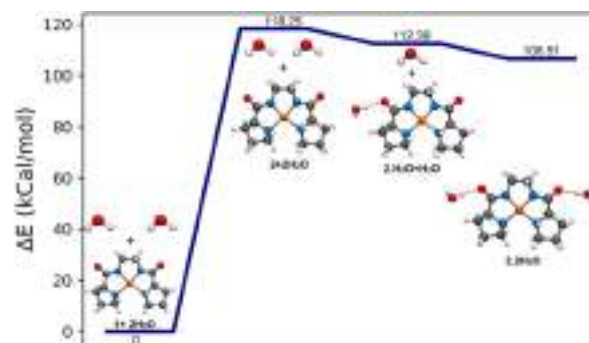

Fig. 7 Energy diagram with total electronic energy and optimized minimum energy structures. The energy of the Cu(II) complex was subtracted from each of the other energies to obtain the diagram. The total electronic energies were calculated at the B3LYP level of theory and 6-311+G(d,p) basis functions with D3 dispersion corrections and using water as a solvent.

it is evident that adding water molecules to **2** stabilizes it. To investigate whether further addition of water molecules continues to stabilize the complex, we tried to optimize various structures with four or six water molecules bound to the carbonyl group of the complex. In Fig. 8, we report some of the structures obtained after optimization. Regardless of the starting geometries, our findings indicate that a maximum of two water molecules bind to each carbonyl atom. Beyond this point, introducing additional water molecules results in forming a hydrogen bonded network of water surrounding the complex.

In addition to analysing the stability of **2** with water, we have also optimized **1**·2H$_2$O. We found that while **2** gets stabilized by 11.73 kcal mol^{-1} when two water molecules are hydrogen bonded to the carbonyl groups on either side, **1** gets stabilized by 15.7 kcal mol^{-1}. We can therefore conclude that solvent interactions stabilize both the Cu(II) and *formal* Cu(III) complexes.

Furthermore, we proceeded to analyse the molecular orbitals of the complexes in cases where one or two water molecules are hydrogen bonded to the carbonyl groups. It is evident from Fig. 9 that as Cu(II) oxidizes to *formal* Cu(III), the HOMO of the Cu(II) complexes becomes the LUMO of the *formal* Cu(III) complexes.

The energy of these orbitals increases from Cu(II) complexes (approximately −5.7 eV, LUMO) to Cu(III) complexes (approximately −4.3 eV, HOMO), and the HOMO–LUMO gap decreases from approximately −2.9 eV in Cu(II) complexes to approximately −5.56 eV in Cu(III) complexes. Additionally, it was observed that the inclusion of one or two water molecules has only a minimal effect on the HOMO–LUMO gap, despite the fact that the addition of water stabilizes the complexes energe-

tically (refer to Fig. 7). Based on these observations, we conclude that Cu(III) complexes are more likely to gain electrons and exhibit higher chemical reactivity. Additionally, the incorporation of hydrogen-bonded water molecules results in an augmented HOMO–LUMO gap, resulting in the stability of both Cu(II) and Cu(III) complexes in water.

After analyzing the molecular orbitals of the Cu(III) complexes, we performed Natural Bonding Orbital (NBO) analysis to evaluate the oxidation state of copper. The NBO analysis revealed that Cu in **2** has a mixed d^9–d^{10} character (4s$^{0.31}$ 3d$^{9.34}$ 4p$^{0.31}$) and a natural charge of +1.026. We also examined the orbital composition of the frontier orbitals and found that the contribution of Cu 3d orbitals in all cases was less than 40% (Table S3†). These findings align with the literature on inverted ligand field theory,[30–33] suggesting that the oxidation state of Cu in intermediate **2** might not be +3 and that the Cu (III) designation should be considered as indicating only a *formal* charge of +3.

Reactivity with phenols

The reaction of **2** with phenol and its derivatives was investigated in H$_2$O : CH$_3$CN (1 : 1) at 25 °C. In the case of monosubstituted phenols, the decay rate is slower, so we employed pseudo-first-order conditions (excess substrate). However, we observed the faster decay rates of tri-substituted phenols like 4-X-2,6-di-*tert*-butylphenol (X = H and OMe), allowing us to use stoichiometric conditions. With excess substrate, the pseudo-first-order reactions were carried out, and the decay rate of the absorbance at 414 nm of **2** fits appropriately with a single exponential decay function. This corresponds to the first-order decay rate based on a single-step kinetic process. The plot of k_{obs} *vs.* [ArOH] was fitted with linear regression, producing a good linear dependence, and the slope of these fits yielded a second-order rate constant k_2 (Table 1 and Fig S19–S24†). The k_2 values show that the reaction rate increases as the O–H bond dissociation energy decreases (Fig. 10). It was observed that the rate of phenol substrate oxidation by **2** dramatically decreases in water compared to previously reported reactivity in MeOH : CH$_3$CN (Table 1). From Table 1, it was apparent that k_2's of 4-OMe-2,6-DTBP and 2,6-DTBP measured in water at 25 °C are similar to the reported values obtained in MeOH : CH$_3$CN (1 : 20) at a much lower temperature, *i.e.*, −30 °C. The decrement in the reactivity probably originates from a decrease in the electrophilic nature of **2**.

Furthermore, we conducted a Hammett analysis to comprehend the nature of the intermediate involved. The negative slope (−1.24) observed from the Hammett analysis also indicates that the reaction pathway involves hydrogen atom transfer (HAT). The slope in the aqueous medium (−1.24) is less negative than that observed in the organic solvent CH$_3$CN (−1.90). This less negative slope suggests a decrease in the electrophilic character of Cu(III), leading to a decrease in reactivity (Fig. 11).[34]

To understand the mechanistic pathway for phenol oxidation, we obtained a Bell–Evans–Polanyi plot (BEP) by plotting $\Delta G^{\ddagger}$ *vs.* BDE$_{O–H}$, where $\Delta G^{\ddagger}$ is Gibbs energy of activation
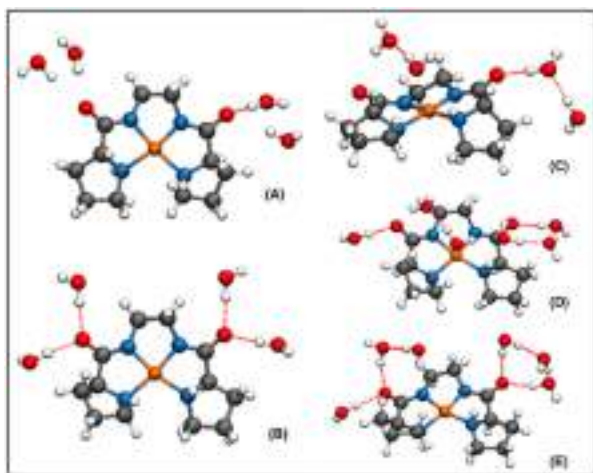

Fig. 8 Optimized structures obtained by increasing the number of hydrogen bonded water molecules. In all the cases, optimization was started from an initial geometry where the two carbonyl oxygen atoms of **2** were each hydrogen bonded to two or three water molecules. In figures A–C, we show structures obtained after optimizing with a total of four water molecules and in D and E, we show structures obtained with six water molecules.
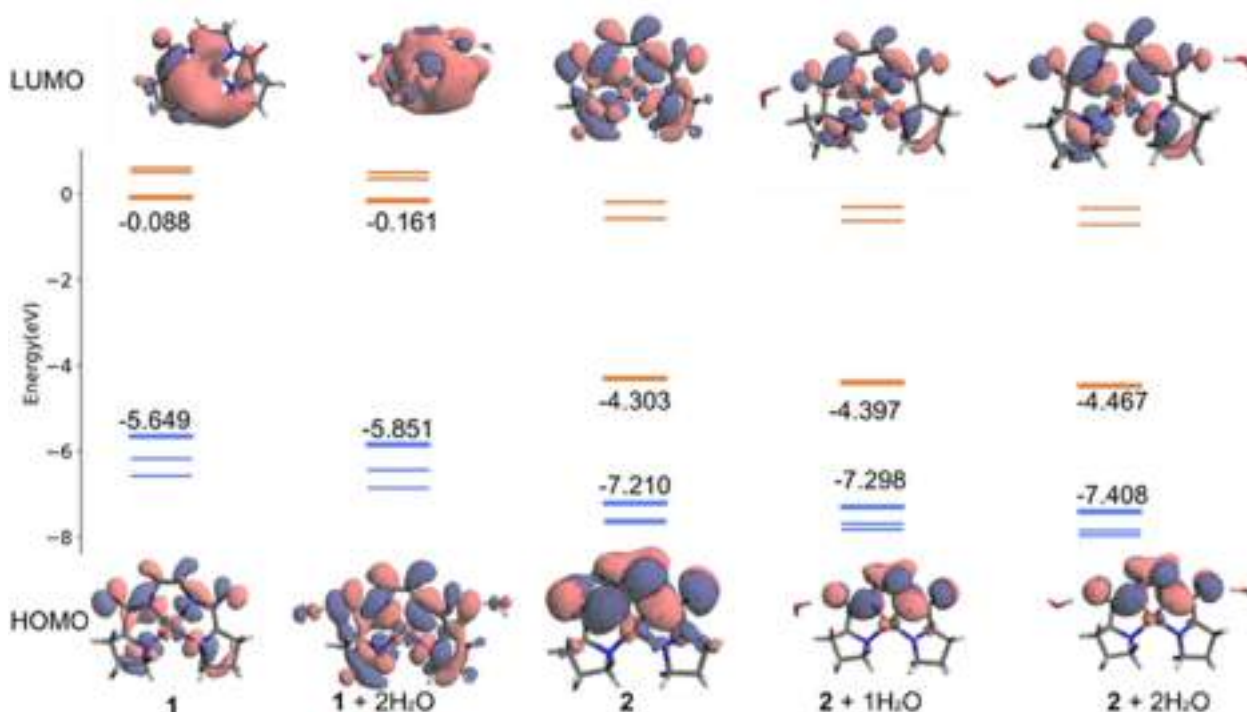
Fig. 9 The molecular orbitals: HOMO−2 (blue thin lines), HOMO−1 (blue thin lines), HOMO (blue thick lines), LUMO (brown thick lines), LUMO+1 (brown thin lines), and LUMO+2 (brown thin lines) for 5 systems. Energies (in eV) for the HOMO and LUMO are reported near the band. The energy difference between the HOMO and LUMO is much less for the Cu(III) complexes than for the Cu(II) complex. Red and blue denote positive and negative lobes of the orbital, respectively.

Table 1 Second-order rate constants and BDE of substituted phenols

Substrate	$2\ k_2{}^a$ $(M^{-1}\ s^{-1})$	$2\ k_2{}^b$ $(M^{-1}\ s^{-1})$	BDE^c $(kcal\ mol^{-1})$
4-OMe-2,6-DTBP	160	151.8	78.3
2,6-DTBP	69	82.01	82.8
4-^{t}Bu-phenol	35	11.22	86.5
Phenol	24	2.28	88.3
4-Cl-phenol	11	1.57	90.3
4-Br-phenol	10	1.44	90.7

^{a} Measured at 20 °C in this work. ^{b} Measured at −30 °C as in ref. 22. ^{c} BDE values of substrates were taken from ref. 35.
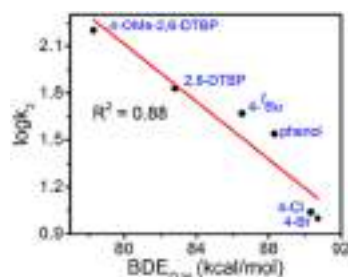

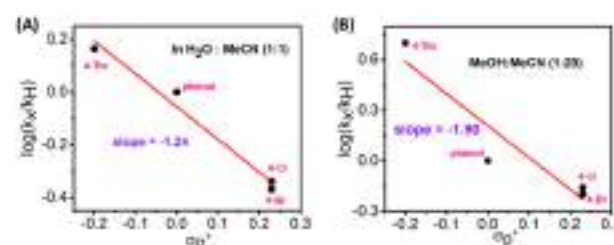**Fig. 11** Hammet plot: substitution constant of various para-substituted phenols vs. $\log(k_x/k_H)$ (A) in $H_2O : CH_3CN$ (1 : 1) and (B) $MeOH : CH_3CN$.

Fig. 10 The plot of BDE_{O-H} vs. $\log k_2$ for the reaction of **2** with various phenols.

obtained from k_2 values and BDE_{O-H} is the strength of the O–H bond in phenols (see the ESI for details†). Upon analysing the BEP plot of **2**, we observed a slope of 0.13 in water and 0.24 in the $MeOH : CH_3CN$ (1 : 20) mixture. It is worth noting that the BEP plot slope for HAT reactions typically lies between 0.15 and 0.70.[36–38] Our data also fall within the range reported for the slopes of BEP plots (Fig. 12). However, the ideal slope for the HAT pathway is 0.5. In the current analysis the slope deviates from the ideal value.[38] Additionally, the reaction of Cu(III) with phenols resulted in the formation of meta-stable radicals, supported by the appearance of their characteristic absorption bands in UV/Vis spectroscopy, leading us to propose an HAT mechanism.
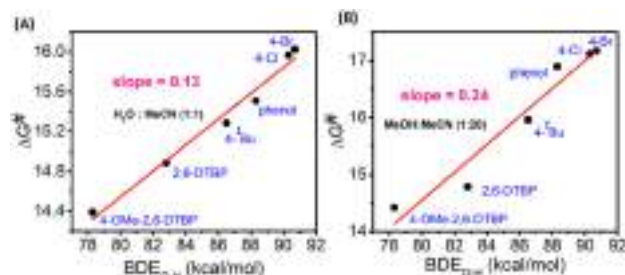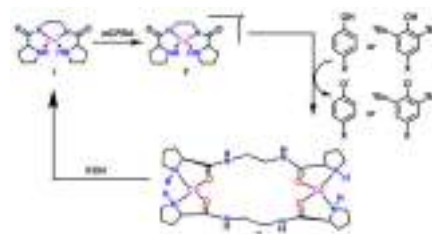

Fig. 12 Bond dissociation energy of various phenols *vs.* Gibbs energy of activation (A) in $H_2O : CH_3CN$ (1 : 1) and (B) in $MeOH : CH_3CN$ (1 : 20).

Scheme 1 Proposed mechanism for the reaction of phenols with **2**. The source of additional protons is either water or *m*-chlorobenzoic acid.

It is reported in the literature that the oxidation of phenols tends to give metastable phenoxyl radicals, which can easily be characterized by UV/Vis absorption spectroscopy. The reaction of 2,6-DTBP with **2** at 25 °C leads to decay at 414 nm, and a new band formation takes place at 420 nm, which is a characteristic band for DPQ (3,3′,5,5′-tetra-*tert*-butyldiphenoquinone) (Fig. S25B†). It was known from the literature that the initially formed 2,6-DTBP˙ radical undergoes dimerization to give DPQ as an end product. The reaction of 4-OMe-2,6-DTBP with **2** showed a new absorption band at 408 nm, which is assigned to the metastable 4-OMe-2,6-DTBP˙ species (Fig. S25C†). This metastable radical further undergoes dimerization to give 2,6-di-*tert*-butyl-1,4-benzoquinone (BQ) as an end product.[13] Furthermore, we have characterized the quantitative transformation of 2,6-DTBP and 4-OMe-2,6-DTBP into DPQ and BQ, respectively, using ^{1}H NMR studies (Fig. S26–S29†). The reaction of the phenol substrate upon treatment with **2** gave a new band at 398 nm, showing the formation of a phenoxyl radical (Fig. S23A†).[22] Notably, our attempts at isolating the product upon a reaction of phenol and mono-substituted phenols were unsuccessful. A similar observation was also reported by Tolman and co-workers.[39]

Interestingly, intermediate **2**, after oxidizing phenols, undergoes reduction to yield a blue-colored dicopper species, $[(LH_2)Cu(II)]_2^{2+}$ (**3**). The addition of 3 eq. of KOH to **3** resulted in the formation of **1**, representing an acid–base equilibrium between **1** and **3** (Fig. S31†). The formation of the end product **3** after the HAT suggests that the ligand played a cooperative role in the oxidation of phenol, wherein the Cu(III) center is involved in an electron transfer reaction and a proton is transferred to the ligand (Scheme 1).

Biological studies

The redox capacity of copper metal ions is always attractive in cancer drug discovery.[40,41] Recently, the modulation of copper metal ions in hundreds of cancer cell lines, including triple-negative breast (TNB) cancer cells, has been shown to prevent cancer cell growth.[42–44] For example, copper ion depleting nanoparticles are shown to disrupt mitochondrial function and enhance oxidative stress to induce apoptosis in TNB cells.[42–44] In parallel, enhancing intracellular copper levels using copper ionophores (eleclomol) was demonstrated to affect mitochondrial respiration and induce proteotoxic stress by accumulating aggregated lipoylated protein.[43] While these studies contradict each other in terms of copper concentration in cells, they converge at the point where they induce oxidative stress through mitochondrial functional impairment.[42,44] Therefore, we hypothesized that the well-studied redox behavior of our Cu(II) complex (**1**) in water could potentially induce oxidative stress in cancer cells and prevent their proliferation.

To test our hypothesis, we first assessed the effect of **1** on the mitochondrial membrane potential (MMP) of Huh-7 cells using a potentiometric TMRM (tetramethylrhodamine) assay.[45] TMRM, a potentiometric fluorescent probe, turns on when accumulated in the active mitochondria of a live cell; however, the fluorescence is lost when mitochondria are impaired. We observed a sharp decrease in the MMP upon treatment with **1**, comparable to that of the positive control H_2O_2. A combination of **1** with H_2O_2 produced comparable or slightly enhanced deterioration of the MMP in Huh-7 cells.

Conversely, antioxidants such as vitamin E (Vit-E) or *N*-acetylcysteine (NAC) were found to protect or recover the MMP when combined with **1** under comparable conditions (Fig. 13A). The observations also reflected in the quantification of the fluorescence intensity under the treatment conditions (Fig. 13B). The redox switch observed with *m*CPBA for **1** *in vitro* (Fig. 4) is predicted to enhance ROS in cells. Indeed, our analysis of intracellular ROS accumulation (using H_2-DCFDA oxidation) assay with fluorescence imaging and its quantification has confirmed the effect (Fig. 13C and D), and the Amplex Red assay® also indicated minimal extracellular H_2O_2 accumulation (Fig. 13E).[46] Furthermore, the effect of intracellular enhanced oxidative environment on DNA damage was assessed by monitoring the phosphorylation of DNA damage repair protein, H2AX, at the gamma position (γH2AX).[47] Our data suggested no significant punctum formation compared to that with the positive control doxorubicin, thereby eliminating DNA damage as the target mechanism (Fig. 13F and G). Overall, we find that our complex enhances oxidative stress in cancer cells, which was further enhanced when combined with H_2O_2 and attenuated when combined with antioxidants (vitamin-E or NAC).

Finally, we proceeded to assess the effect of oxidative stress induced by **1** on the viability of Huh-7 cells. Therefore, we investigated the antiproliferative potential of the ligand and
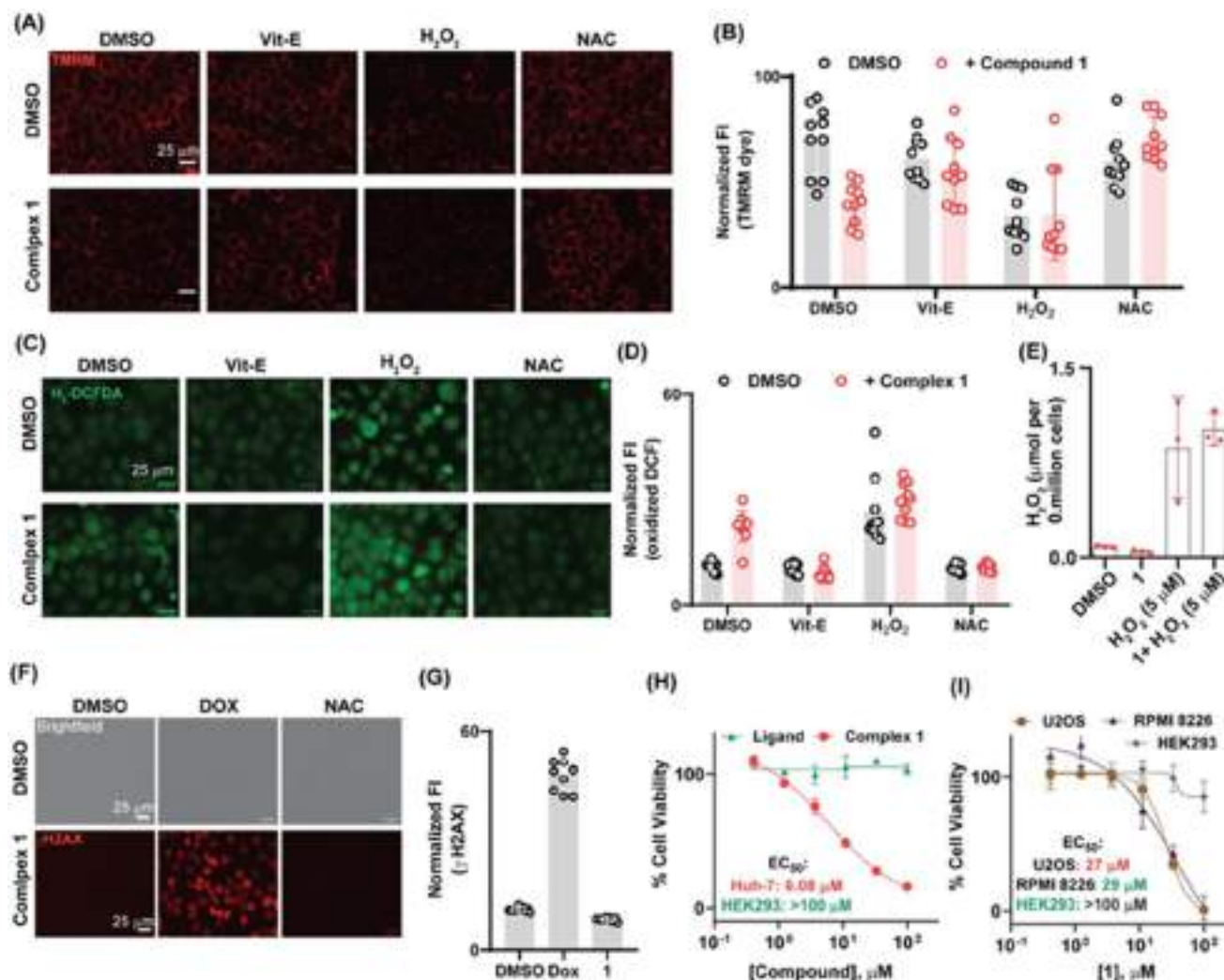
Fig. 13 Evaluation of **1** for antiproliferative activity in cancer cells and its mechanisms of action. (A and B) Mitochondrial membrane depolarization upon treatment with **1** and controls for 90 min and captured using TMRM fluorescence imaging assay in Huh-7 cells and its quantification. (C and D) Intracellular H_2O_2 generation was visualized using H2-DCFDA oxidation fluorescence imaging assay in Huh cells after 90 min of treatment under indicated conditions and its quantification. (E) Extracellular H_2O_2 was quantified and measured using a fluorescence readout based Amplex Red® assay. (F and G) DNA damage analysis using immunofluorescence imaging for γH2X in Huh-7 cells upon treatment with **1** and the quantified data. (H and I) Cell viability analysis of (H) Huh-7, (I) HEK293, U2OS, and RPMI 8226 was performed using resorufin reduction assay after 72 h of treatment with indicated molecules.

copper salt ($CuCl_2$) independently and the ROS generating complex **1** with Huh-7 cells, which was exposed to our molecules at the indicated doses for 72 h (Fig. 13H and I). We observed **1** exhibiting an EC_{50} of 6 μM; however, the lone treatment of Huh-7 cells with either $CuCl_2$ or a ligand was nontoxic even at 10 and 100 μM concentrations, respectively. We have also assessed the toxicity of **1** to a couple more cancer cell lines, osteosarcoma (U2OS) and leukaemia (RPMI 8226) cancer cells, and found that they showed a weak EC_{50} in the range of 27–29 μM (Fig. 13H). Interestingly, **1** showed no toxic effect in normal kidney cells (HEK293) up to 100 μM (Fig. 13I). Together, our biological investigation has revealed that the copper complex **1** can prevent cancer cell growth, particularly with selectivity to liver cancer cells (Huh-7), through the induction of oxidative stress impacting mitochondrial function.

Conclusion

Motivated by how the metalloenzymes utilize water as a medium for their functional activity, we characterized a *formal* Cu(III) species supported by a tetradentate pseudopeptide ligand in water at room temperature. Species **2** was characterized by various spectroscopic techniques like UV-Vis, rRaman, EPR, and ESI-MS. Resonance Raman data of **2** revealed a red-shift in the carbonyl stretch by 34 cm^{-1}, probably due to water's hydrogen bonding interactions with amide core oxygen. These hydrogen bonding interactions probably lead to **2**'s stability in water compared to that in acetonitrile.[22] The experimental findings are supported by DFT studies. Species **2** can oxidize various phenols to give either meta-stable phenoxyl radicals or radical-coupled products. This oxidative capacity of

1 exhibited selective antiproliferative activity against liver cancer cells through mitochondrial functional impairment. Furthermore, the complex role as an inhibitor of cancer cell proliferation may help in developing new Cu-based cancer therapeutics.

Experimental section

Spectroscopy

All chemicals and reagents were purchased from commercial sources and were used as received. HPLC water and anhydrous CH_3CN were utilized in spectroscopic studies. The ligand N,N'-(ethane-1,2-diyl)bis(pyrrolidine-2-carboxamide) and (L)Cu(II) complex (**1**) were synthesized following previously reported literature procedures.[22,48] UV/Vis absorption spectroscopy and kinetic experiments were executed using an Agilent 8453 diode-array spectrophotometer. The ESI-MS of **1** and **2** were recorded on an Agilent 6546 LC/Q-TOF in the positive-ion mode. A Bruker EMX 1444 spectrometer equipped with a temperature controller was employed to record the X-band EPR data at 120 K. Simulation of the EPR data was carried out using the Bruker WINEPR SimFonia software. Cyclic voltammetry experiments were carried out at room temperature using a CH Instruments Electrochemical Analyzer M-600B series. A three-electrode system was used where glassy carbon was used as a working electrode, Pt wire was used as an auxiliary electrode, and aqueous Ag/AgCl as the reference electrode. 100 mM KNO_3 in water was used as a supporting electrolyte. Raman spectra were obtained using a λ_{exc} of 457 nm from Cobolt lasers (50 mW Twist, Cobalt lasers) in a 180° backscattering mode. The laser was combined with the optical axis of the spectrometer (Shamrock300i spectrograph equipped with a 1200 l min^{-1} grating blazed at 500 nm and 100 micron slits) with a dichroic mirror (Semrock) and focused onto the sample with a 7.5 mm focal length (2.5 cm diameter) planoconvex lens with Raman scattering collected and collimated by the same lens and passed through a Rayleigh line long pass rejection filter (Semrock) and focused onto the spectrograph with a 7.5 mm focal length (2.5 cm diameter) planoconvex lens. The Raman scattering was dispersed onto an Andor Technology idus-420-BU CCD. The ^1H NMR spectra were obtained using JEOL JNM LA 500 (500 MHz) and JEOL JNM LA 400 (400 MHz) NMR spectrometers. Elemental analysis was characterized using X-ray photoelectron spectroscopy (XPS) with an Auger electron spectroscopy (AES) module PHI 5000 Versa Prob II. The XPS spectrometer was equipped with a monochromatic Al Kα (hn = 1486.6 eV) radiation source. Nanometric gold coating was performed using a Quorum vacuum chamber.

XPS sample preparation method

8 mM complex is prepared in MeOH and 1 eq. of CAN is added to generate the intermediate **2** at room temperature. It is allowed to stir for 60 seconds, and diethyl ether is poured into the reaction mixture which precipitates out the intermediate. The precipitate formed is collected and subjected to XPS analysis.

X-ray crystallography

A single crystal of suitable dimensions was used for data collection. Diffraction intensities were collected on a Bruker APEX-II CCD diffractometer with graphite-monochromated Mo Kα (0.71073 Å) radiation at 100(2) K. Data were corrected for Lorentz and polarization effects; empirical absorption corrections (SADABS v 2.10) were applied. Using Olex2,[49] the structures were solved using the ShelXT26 structure solution program with intrinsic phasing and refined with the ShelXL[50] refinement package using least squares minimization. The non-hydrogen atoms were refined anisotropically, whereas the H atoms fixed to their geometrically ideal positions were refined isotropically. All non-hydrogen atoms were refined with anisotropic thermal parameters by full-matrix least squares procedures on F^2. CCDC 2350533 includes the supplementary crystallographic data for **3**.†

Synthesis of 3 (blue dimer)

The ligand N,N'-(ethane-1,2-diyl)bis(pyrrolidine-2-carboxamide) (100 mg, 0.40 mmol) was dissolved in 4 ml methanol. To the above-prepared solution, 4 ml methanolic Cu $(ClO_4)_2 \cdot 6H_2O$ (145.6 mg, 0.40 mmol) solution was added, and immediately the color changed to blue, and the reaction mixture was stirred for 6 h. After the completion of the reaction the solvent was evaporated to half of its initial volume under reduced pressure and ether was poured to give a blue precipitate which was further filtered and collected as a crude product (60% yield). The blue colored dimeric Cu(II) crystal structure is obtained in a day by dissolving the crude complex in CH_3CN by layering it with toluene (Scheme S1†).

Computational studies

The structures of Cu(II) and Cu(III) complexes, along with different numbers of water molecules hydrogen bonded to these complexes were optimized using Density Functional Theory (DFT).[51] Optimizations and subsequent frequency analysis were carried out using the Gaussian 09 software,[52] at the B3LYP level of theory,[53,54] using DFT-D3 dispersion corrections,[55] and 6-311+G(d,p) basis functions. Additionally, single point energy calculations were performed using the Def2-TZVPP basis set.[56] Water was used as a solvent in all the calculations and the solvent effects were added using the conductor-like Polarizable Continuum Model (CPCM scheme).[57,58]

Biological studies

Statistics and reproducibility. Data were expressed as mean ± s.d., and P values were calculated using an unpaired two-tailed Student's t-test for pairwise comparison of variables with a 95% confidence interval and $n − 2$ degrees of freedom, where n is the total number of samples, in all figures. Each of the biological studies were performed in the Huh-7 cell line and are representative of two or more independent experiments with a minimum of triple technical replicates.

Cell culture. Huh-7, U2OS, and HEK293 were grown in DMEM (Dulbecco's Modified Eagle's Medium, Gibco). RPMI8226 cells were grown in RPMI 1640. DMEM and RPMI medium were supplemented with 10% FBS (Foetal Bovine Serum, Gibco) and 1% PenStrep (Penicillin Streptomycin, Gibco)

Dose-dependent cell viability studies in U2OS, Huh-7, HEK293, and RPMI8226 cell lines by resazurin assay. Cells were cultured in T75 flasks (Thermo Fisher Scientific) until they attained 70%–80% confluency. The cells were trypsinized with 4 mL of trypsin (0.25% trypsin-EDTA, Gibco) and counted using a hemocytometer. In a 384 well plate, 500 cells per well with 75 μL media were plated into 360 wells (Thermo Fisher Scientific). The remaining 24 wells were plated with only media. The plates were incubated at 37 °C with 5% CO_2 (Forma steri cycle CO_2 incubator – Thermo Fisher Scientific) for 24 hours. The cells were treated with 8 different concentrations of **1** in triplicate. The concentrations of the compound were as follows: 100 μM, 33.3 μM, 11.1 μM, 3.7 μM, 1.23 μM, 0.411 μM, 0.137 μM, and 0.045 μM; 0.1% DMSO was used as a negative control, and 533 nM doxorubicin and 5 μM cisplatin positive control conditions were used in the treatment. The cells were incubated for 72 hours at 37 °C with 5% CO_2 after treatment. After 72 hours of incubation, media were discarded from the wells and washed with 1× PBS. 0.02 mg mL^{-1} of resazurin (SRL) was made in DMEM, and 75 μL of resazurin was added to every well of the 384 well plate. After adding resazurin, the cells were incubated in the incubator for 6 h, and fluorescence readings were recorded (excitation wavelength – 520 nm and emission wavelength – 580 nm) in a multimode plate reader. Percentage cell viability was calculated as follows: ((fluorescence of treated cells − fluorescence of media control)/(fluorescence of DMSO controls − fluorescence of media control)) × 100. Graphs were plotted by using the non-linear regression curve fit programme of Graphpad Prism 9.0. EC_{50} was calculated using GraphPad Prism software. The data provided are representative of three or four independent experiments.

Mitochondrial membrane potential analysis using TMRM in the Huh-7 cell line. 20 000 cells per well were plated in clear flat bottom 96 well plates (NEST) in 200 μL DMEM for mitochondrial membrane potential analysis. The plates were incubated at 37 °C with 5% CO_2 for 24 hours. After 24 hours of incubation, cells were treated for 90 minutes at 37 °C with 5% CO_2 with 0.02% DMSO, **1** – 20 μM, NAC – 500 μM, *tert*-butyl hydroperoxide – 30 μM, H_2O_2 – 150 μM, α-tocopherol (Vit-E) – 50 μM, **1** + NAC, **1** + H_2O_2, **1** + *tert*-butyl hydroperoxide, and **1** + α-tocopherol (Vit-E). After 90 minutes, compounds from the wells were removed, and the wells were washed once with 100 μL 1× PBS. Each well of Huh-7 cells was treated with 50 μL of media that contained 30 nM tetramethyl rhodamine and methyl ester percholate (TMRM) – (TCI) for 30 minutes at 37 °C with 5% CO_2. After incubation, TMRM was removed from the wells, and the wells were washed with 100 μL 1× PBS twice. 100 μL 1× PBS was added to all wells, and cells were observed under the microscope, and images were captured using a fluorescence microscope (Bio-Rad ZOE fluorescent cell imager). Images were merged using ImageJ software. The data

provided are representative of three or four independent experiments.

ROS quantification by using DCFDA in the Huh-7 cell line. To measure total intracellular ROS levels in Huh-7 cells, 20 000 cells per well were plated in clear flat bottom 96 well plates in 200 μL DMEM. The plates were incubated at 37 °C with 5% CO_2 for 24 hours. After 24 hours, the cells were treated for 90 minutes at 37 °C with 5% CO_2, 0.02% DMSO, **1** – 20 μM, NAC – 500 μM, *tert*-butyl hydroperoxide – 30 μM, **1** + NAC, and **1** + *tert*-butyl hydroperoxide. After 90 minutes, 2 μM 2′,7′-dichlorofluorescein 3′,6′-diacetate (DCFDA) (Thermo Fisher Scientific) (dissolved in DMSO) was directly added to cells and incubated in the incubator for 5 minutes. Media were removed from the wells, and the cells were washed with 100 μL of 1× PBS twice. The cells were observed under a microscope, and images were captured using a fluorescence microscope (Bio-Rad ZOE fluorescent cell imager).

Pγ-H2AX immunostaining:. For the Pγ-H2AX immunostaining experiment in Huh-7 cells, 20 000 cells per well were plated in a clear bottom 96 well plate (NEST) and incubated in the incubator (5% CO_2, 37 °C) for 24 hours. They were treated in triplicate with DMSO, 20 μM **1**, 1 μM doxorubicin, and 500 μM NAC for 2 hours in the incubator. Post-treatment, the cells were washed with 200 μL of ice-cold 1× PBS and fixed with 100 μL of 4% formaldehyde for 15 minutes at room temperature. Then, the cells were washed with 200 μL of ice-cold 1× PBS twice. Then 100 μL of ice-cold 100% methanol was added to the cells and incubated at −20 °C for 10 minutes. Again, the cells were washed thrice with 200 μL of ice-cold 1× PBS. Pγ-H2AX (Cell Signalling Technology) was diluted in a 1 : 50 ratio by using antibody dilution buffer (1% BSA in 1× PBS), and 50 μL of diluted antibody was added to the cells and incubated for 1 hour in dark at room temperature. After staining, the cells were washed thrice with ice-cold 1× PBS, and the cells were observed under a microscope, and images were captured using a fluorescence microscope (Bio-Rad ZOE fluorescent cell imager). The data provided are representative of three or four independent experiments.

Extracellular ROS quantification by using Amplex Red® in the Huh-7 cell line. For the quantification of extracellular ROS, an H_2O_2 standard curve generation experiment was performed. 8 different concentrations of H_2O_2 were prepared in 50 μL of 0.5× PBS in triplicate as follows: 5 μM, 1.6 μM, 0.55 μM, 0.18 μM, 0.061 μM, 0.02 μM, 0.006 μM, and 0.002 μM. 50 μL of 0.5× PBS that contains 100 μM Amplex Red (Thermo Fisher Scientific) and 0.2 U mL^{-1} of Horse Radish Peroxidase enzyme (sigma) (final concentrations – 50 μM Amplex Red and 0.1 U mL^{-1} of HRP) was added to all the wells of the 96 well plate. The fluorescence readings at an excitation wavelength of 530 nm and an emission wavelength of 590 nm were recorded in a multimode plate reader. Fluorescence readings of only 50 μM Amplex Red and 0.1 U mL^{-1} of HRP in 0.5× PBS were subtracted from all fluorescence readings of various concentrations of H_2O_2. The *XY* scatter graph was plotted in Microsoft Excel by taking concentrations of H_2O_2 on the *X*-axis and fluorescence readings on the *Y*-axis (Fig. S32†). A straight-line

equation, $Y = mX + C$, was obtained from the graph. For the measurement of total extracellular ROS, Huh-7 cells were scrapped from the T75 flask, and the DMEM was removed by centrifugation (2000 rpm for 3 minutes). 0.1 million cells in 50 μL of 0.5× PBS per well were plated in a clear bottom 96 well plate (NEST). The cells were treated immediately with **1** – 20 μM, hydrogen peroxide – 5 μM, and the combination of **1** and hydrogen peroxide. 0.02% DMSO was used as a negative control. After treatment, the cells were incubated in the incubator (5% CO_2, 37 °C) for 1 hour. After incubation, 100 μM Amplex Red® and 0.2 U mL^{-1} of HRP (final concentrations – 50 μM Amplex Red® and 0.1 U mL^{-1} of HRP) were added to all the wells and incubated again for 1 hour in the incubator. After incubation, fluorescence readings at an excitation wavelength of 530 nm and an emission wavelength of 590 nm were recorded in a multimode plate reader. Fluorescence readings of only 50 μM Amplex Red and 0.1 U mL^{-1} of HRP in 0.5× PBS were subtracted from all fluorescence readings of various treatment conditions. Concentrations of H_2O_2 under various treatment conditions were calculated using the $Y = mX + C$ equation of the H_2O_2 standard curve, where Y is the fluorescence reading, m is the slope, X is the concentration of unknown H_2O_2, and C is a constant. The data provided are representative of three or four independent experiments.

Data availability

The data that support the findings of this manuscript are available in the article's ESI. CCDC 2350533 includes the supplementary crystallographic data for complex **3**.†

Conflicts of interest

There are no conflicts to declare.

Acknowledgements

References

1 R. H. Holm, P. Kennepohl and E. I. Solomon, Structural and Functional Aspects of Metal Sites in Biology, *Chem. Rev.*, 1996, **96**, 2239–2314.

2 E. I. Solomon, U. M. Sundaram and T. E. Machonkin, Multicopper oxidases and Oxygenases, *Chem. Rev.*, 1996, **96**, 2563–2605.

3 J. P. Klinman, Mechanisms Whereby Mononuclear Copper Proteins Functionalize Organic Substrates, *Chem. Rev.*, 1996, **96**, 2541–2561.

4 J. P. Klinman, The Copper-Enzyme Family of Dopamine β-Monooxygenase and Peptidylglycine α- Hydroxylating Monooxygenase: Resolving the Chemical Pathway for Substrate Hydroxylation, *J. Biol. Chem.*, 2006, **281**, 3013–3016.

5 J. Y. Lee and K. D. Karlin, Elaboration of copper–oxygen mediated C–H activation chemistry in consideration of future fuel and feedstock generation, *Curr. Opin. Chem. Biol.*, 2015, **25**, 184–193.

6 P. H. Walton and G. J. Davies, On the catalytic mechanisms of lytic polysaccharide monooxygenases, *Curr. Opin. Chem. Biol.*, 2016, **31**, 195–207.

7 D. Wang, Y. Li, Y. Zheng and Y. S. Y. Hsieh, Recent Advances in Screening Methods for the Functional Investigation of Lytic Polysaccharide Monooxygenases, *Front. Chem.*, 2021, **9**, 1–12.

8 W. Keown, J. B. Gary and T. D. P. Stack, High-valent copper in biomimetic and biological oxidations, *J. Biol. Inorg. Chem.*, 2017, **22**, 289–305.

9 I. M. Dimucci, J. T. Lukens, S. Chatterjee, K. M. Carsch, C. J. Titus, S. J. Lee, D. Nordlund, T. A. Betley, S. N. MacMillan and K. M. Lancaster, The myth of d^8 copper(III), *J. Am. Chem. Soc.*, 2019, **141**, 18508–18520.

10 H. Liu and Q. Shen, Well-defined organometallic Copper (III) complexes: Preparation, characterization and reactivity, *Coord. Chem. Rev.*, 2021, **442**, 213923.

11 Q. Zhang, S. Tong and M. X. Wang, Unraveling the Chemistry of High Valent Arylcopper Compounds and Their Roles in Copper-Catalyzed Arene C–H Bond Transformations Using Synthetic Macrocycles, *Acc. Chem. Res.*, 2022, **55**, 2796–2810.

12 P. J. Donoghue, J. Tehranchi, C. J. Cramer, R. Sarangi, E. I. Solomon and W. B. Tolman, Rapid C–H Bond Activation by a Monocopper(III)–Hydroxide Complex, *J. Am. Chem. Soc.*, 2011, **133**, 17602–17605.

13 T. Wu, S. N. Macmillan, K. Rajabimoghadam, M. A. Siegler, K. M. Lancaster and I. Garcia-Bosch, Structure, Spectroscopy, and Reactivity of a Mononuclear Copper Hydroxide Complex in Three Molecular Oxidation States, *J. Am. Chem. Soc.*, 2020, **142**, 12265–12276.

14 M. Akbar Ali, P. V. Bernhardt, M. A. H. Brax, J. England, A. J. Farlow, G. R. Hanson, L. L. Yeng, A. H. Mirza and K. Wieghardt, The Trivalent Copper Complex of a Conjugated Bis-dithiocarbazate Schiff Base: Stabilization of Cu in Three Different Oxidation States, *Inorg. Chem.*, 2013, **52**, 1650–1657.

15 P. Garrido-Barros, D. Moonshiram, M. Gil-Sepulcre, P. Pelosin, C. Gimbert-Suriñach, J. Benet-Buchholz and A. Llobet, Redox Metal–Ligand Cooperativity Enables Robust and Efficient Water Oxidation Catalysis at Neutral